We are IntechOpen, the world's leading publisher of Open Access books Built by scientists, for scientists

4,800
Open access books available

122,000
International authors and editors

135M
Downloads

Our authors are among the

154
Countries delivered to

TOP 1%
most cited scientists

12.2%
Contributors from top 500 universities

WEB OF SCIENCE™

Selection of our books indexed in the Book Citation Index in Web of Science™ Core Collection (BKCI)

Interested in publishing with us?
Contact book.department@intechopen.com

Numbers displayed above are based on latest data collected.
For more information visit www.intechopen.com

5

Chemical Sensors Based on Photonic Structures

Vittorio M. N. Passaro, Benedetto Troia,
Mario La Notte and Francesco De Leonardis
Photonics Research Group, Dipartimento di Elettrotecnica ed Elettronica,
Politecnico di Bari,
Italy

1. Introduction

Photonic sensors have been the subject of intensive research over the last two decades for use in civil and military environments, especially for detection of a wide variety of biological, chemical and nuclear agents. Photonic sensor technologies involve a lot of application fields like chemical, temperature, strain, biomedical, electrical, magnetic, rotation, pressure, position, acoustic and vibration sensors. Important efforts have been carried out by the international scientific community (academia, industry-R&D and all interested parties), to develop and improve the know-how and the state-of-the-art of photonic sensing. In this context, optical Lab-on-a-chip systems, based on chemical and biochemical sensors, represent the state of the art of photonic sensing, since they are expected to exhibit higher sensitivity and selectivity as well as high stability, immunity to electromagnetic interference, and product improvements such as smaller integration sizes and lower cost (De Leonardis et al., 2007).

In recent years, rapid advancements in photonic technologies have significantly enhanced the photonic biochemical sensor performance, particularly in the areas of light – analyte interaction, device miniaturization and multiplexing, and fluidic design and integration. This has led to drastic improvements in sensor sensitivity, limit of detection, advanced fluidic handling capability, lower sample consumption, faster detection time, and lower overall detection cost per measurement. This trend is not a casual phenomenon, indeed it justifies the economic interest that many industries reveal to photonic chemical and biochemical sensors. With future commercialization of photonic biosensors in lab-on-a-chip systems, next generation biosensors are expected to be reliable and portable, able to be fabricated with mass production techniques to reduce the cost as well as to do multi-parameter analysis, enabling fast and real-time measurements of a large amount of biologic parameters within a single, compact sensor chip. For example, needs are expected to be boosted by healthcare, such as the increasing prevalence of diabetes in the population and the growing demand for home and point-of-care testing and monitoring tools.

In conclusion, optical biosensors (Passaro et al., 2007a) have reached a high degree of maturity in crucial areas of application such as environmental monitoring, biotechnology, medical diagnostics, drug screening, food safety (Arshak et al., 2009), and security (Leheny & McCants, 2009).

2. Photonic bio-chemical sensors: Sensing principles and architectures

A chemical sensor can be defined as an analytical device that coverts chemical or bio-chemical information (e.g., concentration, composition analysis), into a quantifiable and processable signal.

One of the possible chemical sensor classifications, concerns with the principle of the transducer, i.e. the device that transforms the chemical information about the sample (chemical analytes, molecules, cells or gases), into an analytical signal. To this purpose, electrochemical, electrical, mass sensitive, magnetic, thermometric and optical sensors can be classified as different types of chemical sensors.

A photonic chemical sensor is characterized by an optical-based transduction. This one includes a large number of sensing principles based on absorption, reflection, refraction, dispersion, Raman effect, chemiluminescence, fluorescence and phosphorescence, to name a few. The general scheme of a photonic chemical sensor can be represented as in Fig. 1 below.

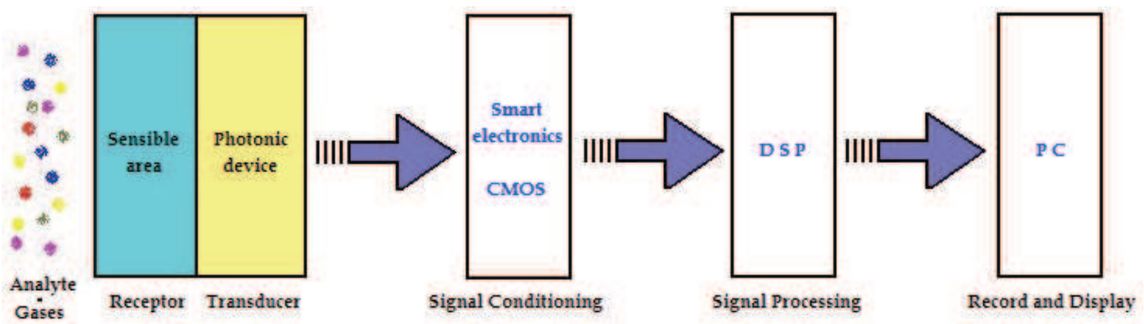

Fig. 1. Schematic diagram of a photonic bio-chemical sensor.

Colored blocks named "Sensible area" and "Photonic device", represent the receptor and the transducer of the photonic biochemical sensor, respectively.

The receptor is a fundamental part of the sensor. In fact, it has to be designed in order to catalyze the specific chemical reaction or biochemical process, exhibiting a high selectivity for the analyte or the chemical specie to be detected. Generally, the receptor can be realized by covering the sensor surface (sensible area), with polymeric layers (~ nm-thin). These ones are characterized by selective receptors, able to capture and immobilize only one type of analyte in a complex chemical sample (e.g., glucose in blood, metallic particles in water, antigen/antibody in organic solution). By this way, the sensible area is the direct maker of the sensor selectivity and can be defined as a chemical prerogative.

In an intrinsic photonic bio-chemical sensor, the transducer is generally represented by an integrated optical waveguide (e.g., optical fiber, slot-waveguide, photonic crystal waveguide, photonic wire waveguide). By this way, this photonic device has to satisfy different parallel functions. The first one consists in guiding the photonic signal from the optical source (e.g., led, laser), to the sensible area. Consequently, the photonic waveguide has the rule of transducer, enhancing the interaction between the chemical/biochemical process and the optical signal. By this way, the chemical information can be properly transduced into an optical one and, finally, guided to the photo-detector to be transformed into an analytically useful electrical signal. In this context, the transducer can be considered

as an engineering prerogative, because several technical solutions have to be implemented in order to maximize the confinement of the optical field in the sensible area.

The remaining blocks labeled as "signal conditioning" and "signal processing", represent the sensor front-end, generally identified by integrated digital/analog CMOS electronics. The electrical signal obtained by the conversion of the photonic one, has to be restored by amplification and filtering, then processed in order to decode the analyte (chemical) information to be recorded and displayed ("record and display").

Intrinsic photonic biosensors are generally integrated chips, characterized by small footprints (~ mm^2, ~ μm^2). On the contrary, in extrinsic photonic biochemical sensors the waveguide does not directly interact with the chemical/biochemical process. In fact, the photonic waveguide cannot represent the transducer because it is designed only to able the optical signal propagation. Extrinsic photonic sensors can be classified as "benchtop" systems. They are expensive and not suitable for mass-scale production. In addition, they are characterized by large dimensions and low portability.

Nowadays, integrated photonic chemical sensors represent the state-of-the-art of photonic sensing. In fact, these sensing systems exhibit ultra high performance and can be realized by standard fabrication processes available in Microelectronics industry (e.g., photolithography and ICP etching). Consequently, additional start-up costs to be invested in clean room equipments updating are not needed, and mass-scale production can represent a concrete business.

The most popular technological platform adopted for the fabrication of integrated photonic sensors is called silicon-on-insulator (SOI). This one works by placing a thin, insulating layer, such as silicon dioxide or glass, between a thin layer of silicon and the silicon substrate. In Fig. 2 a typical SOI rib optical waveguide designed at 1.55 µm (operative wavelength, λ_{op}) is shown. Both quasi-TE and quasi-TM optical field distributions are plotted.

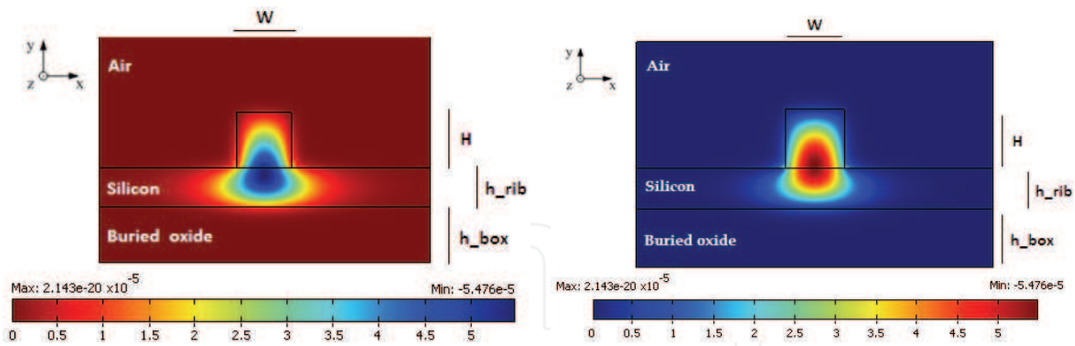

Fig. 2. Optical (a) E_x-field (quasi-TE) and (b) E_y-field (quasi-TM) distributions in a SOI rib waveguide (λ_{op} = 1.55µm, W = 1µm, H = 1µm, h_rib = 700nm, h_box = 1µm).

In particular, it is possible to recognize the insulating layer (SiO_2) characterized by a refractive index n_{SiO2} = 1.45, and built on the silicon substrate (bulk).

A thin silicon layer (n_{Si} = 3.45 @ 1.55 µm) is properly etched in order to realize the rib waveguide, covered by air (n_{air} = 1). The architecture presented above exhibits a good optical transverse electric (TE) and transverse magnetic (TM) field confinement in the rib

structure, directly exposed to the cover medium and characterized by the highest refractive index n_{Si}. However, in both quasi-TE and quasi-TM modal distributions, the optical field is quasi entirely confined in the high index region, reducing the interaction with analytes or gases in the cover medium. To this purpose, other SOI-based waveguide architectures, such as the SOI photonic wire waveguide sketched in Fig. 3, can be adopted in order to improve the field confinement in the cover medium, as well as the interaction between the propagating optical field and the chemical/biochemical species, then resulting in an optimized transduction process.

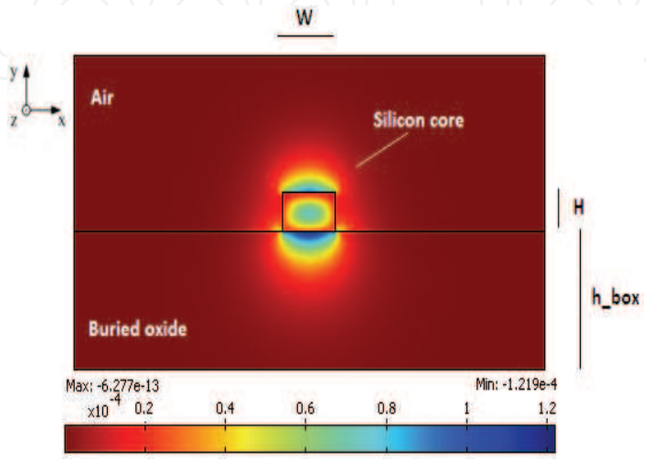

Fig. 3. Optical E_y-field distribution in a silicon-wire waveguide (quasi-TM), λ_{op} = 1.55μm.

In this specific waveguide configuration (h_box = 2μm, W = 450nm, H = 250nm), the optical transverse magnetic (TM) field is concentrated at both interfaces between the high refractive index region (silicon core) and the low refractive index ones (air at the upper side and SiO_2 at the bottom one). By this way, photonic wire waveguides represent a better choice if compared with previously analyzed rib ones. For an electromagnetic wave propagating in the z direction (Fig. 3), the major E-field component of the quasi-TM eigenmode undergoes a discontinuity at the horizontal silicon wire interfaces that, according to Maxwell's equations, is determined by the following relation:

$$\left|\frac{E_L}{E_H}\right| = \left(\frac{n_H}{n_L}\right)^2 \tag{1}$$

In Eq. 1 E_L is the component of the E-field, evaluated in the low refractive index (n_L) region, while E_H is the same component in the high refractive index (n_H) region. In particular, the greater the refractive index contrast $\Delta n = n_H - n_L$, the higher the E_L-field confinement. In this context, SOI technology represents a suitable solution for photonic sensing because it is possible to obtain a high refractive index contrast Δn ($n_{Si} - n_{SiO2} \approx 2$ @ 1.55 μm).

By using one of the two SOI-based waveguides described in the section above, it is possible to realize an intrinsic photonic biosensor. In particular, two different sensing principles characterizing the operating regime of a photonic chemical sensor can be used, i.e. surface and homogeneous sensing (Dell'Olio & Passaro, 2007).

In surface sensing a change of the modal effective index n_{eff} of the propagating optical signal is due to a change of thickness of an ultra-thin layer of selective receptor molecules which are

immobilized on the functionalized waveguide surface. In particular, when the photonic sensor surface is exposed to a complex chemical solution, only target molecules will be recognized by selective receptors and will contribute to the bio-chemical process. By this way, if the thickness of the sensor surface layer was ρ_0 before the exposure to the chemical sample, the thickness of the same layer will be greater, for example $\rho_0 + \rho_1$, after the selective analyte adsorption. The thickness change $\Delta\rho$ can be transduced in an effective index change Δn_{eff}.

In homogenous sensing, the modal effective index change is produced by a change of cover medium refractive index, n_c. For example, by assuming that the photonic sensor is initially exposed to air ($n_{air} = 1$ @ 1.55μm), when a specific gas (e.g., He, CO_2, Ar, N_2, C_2H_2) will cover the sensor surface, a sensible cover refractive index change Δn_c will be induced. In addition, the same analysis can be carried out if the sensor is initially covered by water ($n_{water} = 1.33$ @ 1.55μm) and subsequently exposed to another liquid solution (e.g., NaCl). In Table 1 it is possible to appreciate the relative effective index changes under different operative conditions (De Leonardis et al., 2011).

RI Cover medium	RI Gas/Liquid	Δn_C (%)
$n_{air} = 1$	$n_{He} = 1.000035$	0.0035
$n_{air} = 1$	$n_{CO2} = 1.000059$	0.0059
$n_{air} = 1$	$n_{Ar} = 1.000278$	0.0278
$n_{air} = 1$	$n_{N2} = 1.000294$	0.0294
$n_{air} = 1$	$n_{C2H2} = 1.000593$	0.0593
$n_{water} = 1.33$	$n_{NaCl} \approx 1.33$	0.0018[1]

Table 1. Refractive index (RI) changes in homogeneous sensing for different gas and aqueous solution concentrations. All data are referred to $\lambda_{op} = 1.55$μm.

Integrated silicon wire waveguides define a class of photonic chemical sensors called "photonic wire evanescent field" (PWEF), because of the interaction between the evanescent optical field and the chemical/biochemical process to be detected (see Fig. 4).

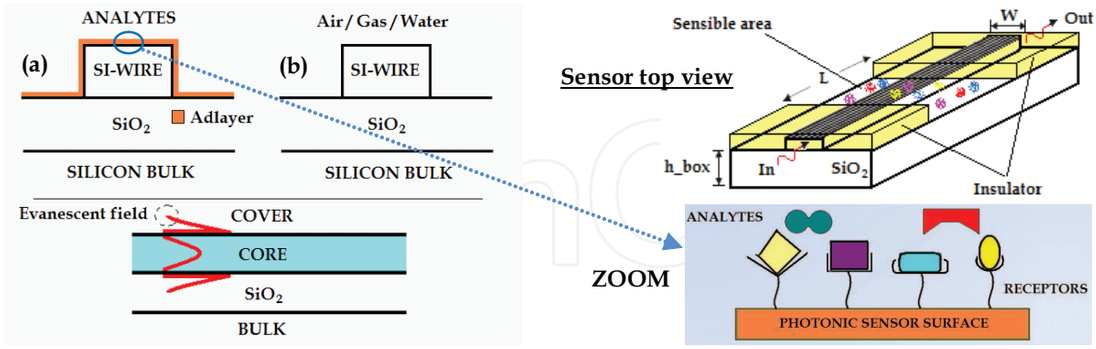

Fig. 4. Schematic representation of surface (a) and homogeneous (b) sensing in a SOI-based wire waveguide.

In both homogeneous and surface sensing it is possible to define an important performance parameter of the photonic chemical /biochemical sensor: the sensitivity.

[1] The refractive index of a NaCl aqueous solution changes 0.0018 RIU per 1% mass concentration (Sun et al., 2009).

$$S_h = \frac{\partial n_{eff}}{\partial n_c}, S_s = \frac{\partial n_{eff}}{\partial \rho} \tag{2}$$

In homogeneous sensing, according with variational theorem for dielectric waveguides, it is possible to write:

$$S_h = \left.\frac{\partial n_{eff}}{\partial n_c}\right|_{n_C = n_C^0} = \frac{2n_C^0}{\eta_0 P}\iint_C \left|\vec{E}(x,y)\right|^2 dxdy = \frac{2n_C^0 \Gamma_C}{\eta_0 P}\iint_\infty \left|\vec{E}(x,y)\right|^2 dxdy \tag{3}$$

where

$$P = \iint_\infty \left[\left(\vec{E}\times\vec{H}^* + \vec{E}^*\times\vec{H}\right)\bullet\hat{z}\right]dxdy \tag{4}$$

η_0 is the free space impedance (377Ω), $\vec{E}$ and $\vec{H}$ are the electric and magnetic field vectors, respectively, n_c^0 is the unperturbed value of cover medium refractive index, $\hat{z}$ indicates the unit vector along z direction (propagation direction) and Γ_C is the confinement factor in the cover medium (Dell'Olio & Passaro, 2007).

In surface sensing, shift of n_{eff} (Δn_{eff}) due to a change $\Delta\rho$ of ad-layer thickness can be calculated by using a perturbation approach as:

$$\Delta n_{eff} = \frac{n_m^2 - \left(n_C^0\right)^2}{\eta_0 P}\iint_M \left|\vec{E}(x,y)\right|^2 dxdy \tag{5}$$

where n_m is the molecular ad-layer refractive index and M is the region in which the ad-layer increases. Surface sensitivity S_s, can be calculated by using the definition in Eq. 2.

In conclusion, there is a last consideration concerning with units of measurement of both analyzed sensitivities, S_h and S_s. In the first case, the performance parameter S_h is dimensionless, because it is the ratio of two dimensionless physical quantities. On the contrary, surface sensitivity is generally measured in nm^{-1}, because the ad-layer due to analyte or molecules adsorption is characterized by a nanometer-scale thickness (2-5 nm).

Sensor limit of detection (LOD) represents another important parameter to characterize the sensor performance. It indicates the minimum resolvable signal and can be defined by taking into account the noise in the transduction signal (σ) and the sensor sensitivity (S). Generally, LOD can be calculated as the ratio σ/S.

Photonic chemical sensors based on homogeneous and surface sensing are generally defined RI-based sensors, because the transduction process consists always in a modal effective index change, as previously described. However, there is another class of chemical sensors based on optical absorption detection. In particular, the absorption coefficient, usually indicated with the variable α (cm^{-1}), depends on the operative wavelength of the photonic signal and material (e.g., gas, solid, liquid solutions) electronic and optical properties. For example, fundamental vibrational and rotational modes associated with most inorganic and organic molecules are spectroscopically accessible within the mid-infrared range (mid-IR). By this way, the interaction between mid-IR photons and organic molecules provides particularly sharp

transitions, which, despite of the wide variety of organic molecules, provide unique mid-IR absorption spectra. Therefore, it is possible to reflect the molecularly characteristic arrangement of chemical bonds within the probed molecules via the frequency position of the associated vibrations and mixed rotational-vibrational transitions. In addition to this, a lot of environmental harmful gases like carbon dioxide (CO_2), methane (CH_4) and sulfur dioxide (SO_2), to name a few, are characterized by absorption spectra in mid-IR, as sketched in Fig. 5.

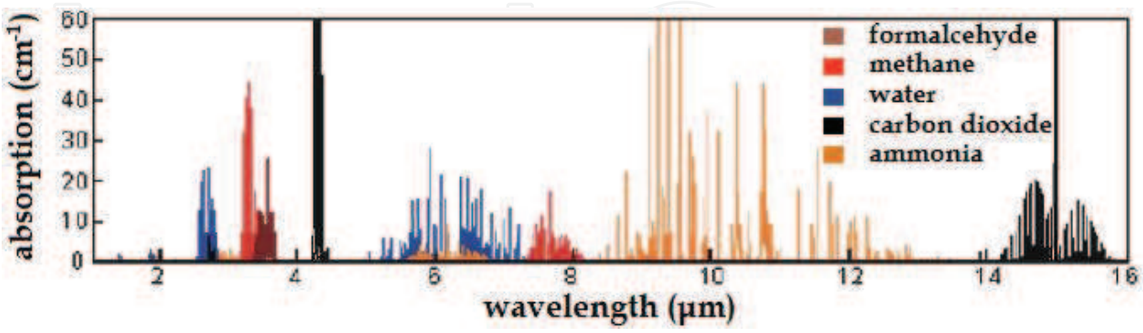

Fig. 5. Absorption spectra of several gases and liquid solutions.

It is possible to detect specific gas species or chemical analytes with high sensitivity and selectivity, by analyzing the transmission spectra of the light intensity in a suitable wavelength range. In particular, the photonic signal intensity is linked to the gas or analyte concentration C via the Beer-Lambert law:

$$I = I_0 \exp(-\alpha L) \tag{6}$$

where I is the light intensity at the end section of the whole path length (L), α linearly depends on C and I_0 is the light intensity at the initial section of the sensible area of photonic sensor. By this way, the sensor readout is an optical intensity one, thus it will be possible to register steep peaks in the transmission spectra corresponding to specific operative wavelengths, properly selected to be the absorption wavelengths of gas or molecule to be detected. Optical absorption detection allows to design photonic chemical sensors characterized by ultra low LOD (e.g., pg/mm^2, ng/mL^1).

In typical bio-chemical sensors, detection of specific pathogens or proteins require transduction labeling elements, such as fluorescent dyes or radioactive isotope, in order to generate a physically useful signal from a recognition event. For example, in fluorescence-based detection the intensity of the fluorescence indicates the presence of the target molecules as well as their concentration. Although label detection exhibits high sensitivity and ultra low LOD down to a single molecule, labeling chemistry is expensive and time-consuming, and may interfere with the function of bio-molecules. In this context, label-free photonic bio-sensing described in this paragraph, allows to preserve the natural form of target molecules and their natural interaction with selective receptors. In conclusion, label-free photonic sensors nowadays represent a universal platform for biochemical assays.

2.1 Slot-waveguides for sensing applications

Slot waveguides represent a very interesting and promising architecture for photonic chemical and bio-chemical ultra-high performance sensing. In fact, by using slot waveguides

it is possible to confine an extremely high optical field in the low refractive index region called "slot region", where the chemical solution or gas will be detected (Almeida et al., 2004; Iqbal et al., 2008). In Fig. 6, it is possible to appreciate the optical field distribution in a silicon slot waveguide and a relative geometrical definition of the slab slot architecture.

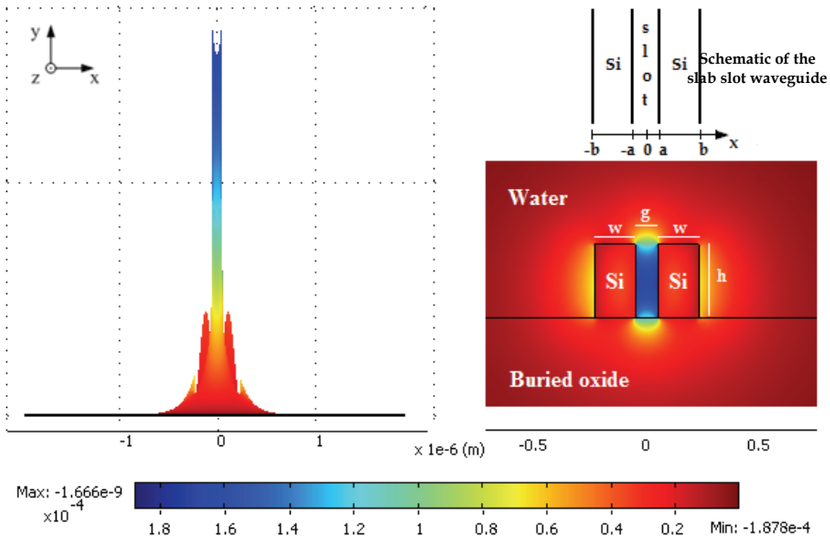

Fig. 6. 2D-views of the E_x-field spatial distribution (quasi-TE) solved for a Si-wire slot waveguide optimized @ 1.55μm; h = 324nm, g = 100nm, w = 180nm.

The mathematical expression of the E_x-field of TM mode in a slab slot waveguide (Fig. 6) is as follows:

$$E_x(x) = A\begin{cases} \dfrac{1}{n_L^2}\cosh(\gamma_S x) & ;|x| < a \\ \dfrac{1}{n_H^2}\cosh(\gamma_S a)\cos\left[k_H\left(|x| - a\right)\right] + \dfrac{\gamma_S}{n_L^2 k_H}\sinh\left[k\left(|x| - a\right)\right] & ; a < |x| < b \\ \dfrac{1}{n_L^2}\left\{\cosh(\gamma_S a)\cos\left[k_H\left(b - a\right)\right] + \dfrac{n_H^2\gamma_S}{n_L^2 k_H}\sinh\left(\gamma_S a\right)\sin\left[k_H\left(b - a\right)\right]\right\}\exp\left[-\gamma_C\left(|x| - b\right)\right] & ; |x| > b \end{cases} \quad (7)$$

where

$$A = A_0\frac{\sqrt{k_0^2 n_H^2 - k_H^2}}{k_0} \quad (8)$$

A_0 is an arbitrary constant, k_0 ($2\pi/\lambda_{op}$) is the vacuum wave number, k_H is the transverse wave number in the high refractive index (n_H) region, γ_C is the field decay coefficient in the cover medium and γ_S is the field decay coefficient in the slot region (low RI region, n_L).

By using slot waveguides instead of PWEF or rib ones, it is possible to enhance the interaction between the propagating optical field and the chemical test sample. In fact, slot-based photonic sensors can exhibit ultra high performance (e.g., $S_h > 1$, LOD $\approx 10^{-4}$ RIU).

To this purpose, interesting results have been presented in literature. For example the slot waveguide optimized for homogeneous sensing and presented in Fig. 6, is characterized by ultra high sensitivity, S_h = 1.0076 for quasi-TE propagation mode. A SOI slot waveguide, (w=135 nm, h=965 nm, g=100 nm) exhibiting ultra-high sensitivity of 1.1, has been also recently demonstrated by the authors. A value $S_h > 1$ implies that an effective index change $\Delta n_{eff} > \Delta n_C$ is induced by a cover index shift Δn_C.

Performance parameters such as sensitivity and confinement factors in cover medium and slot region, depend on waveguide geometrical parameters and materials selected for the fabrication. In fact, in Fig. 7 it is possible to note the sensitivity changes for homogenous sensing as a function of slot height "h", slot region width "g" and wire width "w", in a slot waveguide sensor. By this way, appropriate choice and design of photonic waveguide for chemical or biochemical sensing applications, have to be carried out in order to enhance all performance parameters as mentioned above (Passaro, 2009a).

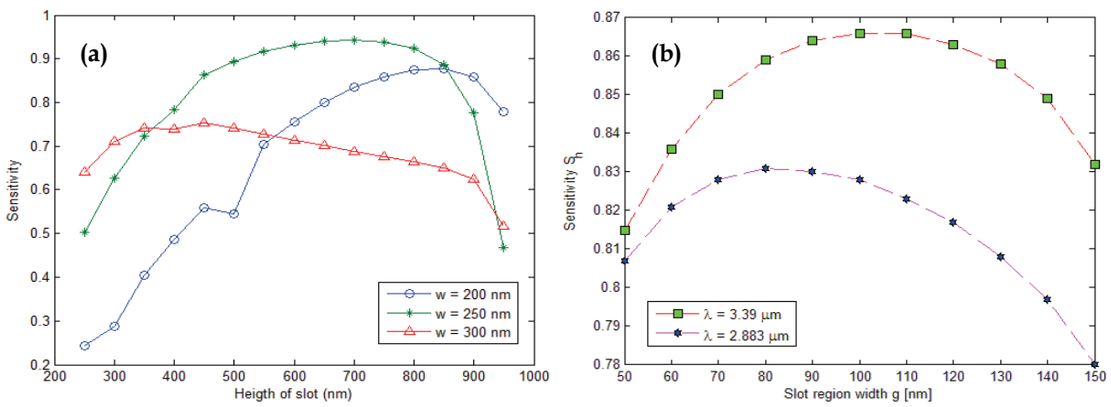

Fig. 7. Slot-waveguide sensitivities for homogeneous sensing as a function of geometrical parameters. (a) Si-on-SiO_2 slot waveguide with air cover optimized @ 1.55μm ($S_{h\text{-}MAX}$ = 0.943, with g = 100nm, w = 250nm, h = 700nm). (b) Si-on-SiO_2 slot waveguide with air cover designed @ 2.883μm (w = 450nm, h = 650nm) and 3.39μm (w = 520nm, h = 800nm).

Nowadays, ingenious design techniques are needed to extend group IV photonics from near-IR to mid-IR wavelength range. In fact, harmful gases like carbon dioxide (CO_2), carbon monoxide (CO), methane (CH_4) and sulfure dioxide (SO_2) are characterized by absorption spectra in mid-IR, specially in the range 2-8μm, according to Fig. 5. To this purpose, several group IV material systems (e.g., SiGe, SiGeSn, SiGeC, GeC, SiSn) have been investigated (Troia et al., 2011). These alloys have been proposed for the design of slot waveguide sensors for homogeneous sensing, working at 3.39μm and 2.883μm. Interesting theoretical performances have been obtained by optimizing SOI-based slot waveguides designed for optical transparency at working λ_{op} and ultra high refractive index contrast Δn. In particular, $S_h > 1$ has been demonstrated for two slot waveguides constituted by group IV material system layers, properly designed and stacked to form symmetrical wires, as sketched in Fig. 8 (Passaro et al., 2011). The most important advantages of these mid-IR "slot" sensors with respect to conventional slot sensors optimized at 1.55μm, concern with higher performance, relaxed fabrication tolerances, and presence of a second-order slot mode, able to be used for sensing. Similar investigations have been also proposed about novel optical slot waveguides working at 2.883μm ($Si_{0.15}Ge_{0.85}/Si/SiO_2$ and $Si_{0.15}Ge_{0.85}/SiO_2$).

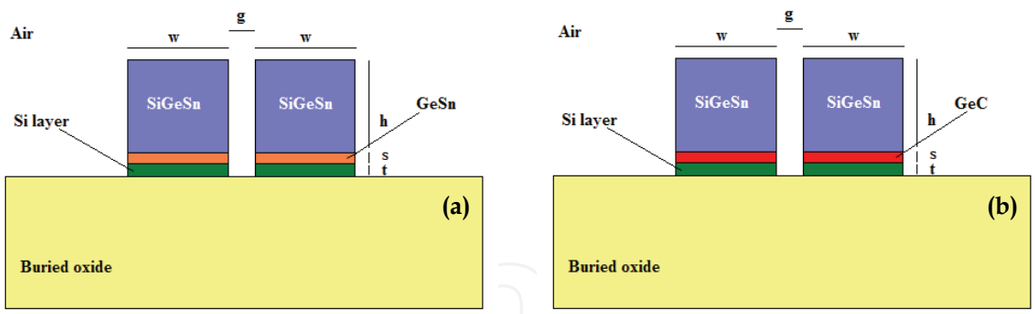

Fig. 8. Optimized novel slot photonic waveguides based on group IV alloys and material systems, designed at λ_{op} = 3.39μm. (a) $Si_{0.08}Ge_{0.78}Sn_{0.14}/Ge_{0.91}Sn_{0.09}/Si/SiO_2$ with w = 380nm, h = 520nm, t = 20nm, s = 50nm, g = 100nm; (b) $Si_{0.08}Ge_{0.78}Sn_{0.14}/Ge_{0.97}C_{0.03}/Si/SiO_2$ with w = 390nm, h = 560nm, t = 20nm, s = 50nm, g = 100nm.

In addition, these slot waveguides exhibit ultra-high performance (S_h > 1, LOD ~ 4×10^{-5}). The most important limitation that characterizes some of these intriguing alloys is the impossibility to grow the analyzed material systems selectively and directly on silicon dioxide. The effect of this limitation imposes some inevitable technological restrictions in the design of above described novel photonic sensors. For example, GeSn and SiGeSn alloys can be grown either on Si(100) or Ge/Si(100) wafers, using the SnD_4, $SiGeH_6$, Ge_2H_6 and Si_3H_8 hydride compounds as a source of Sn, Ge and Si constituent atoms, respectively. However, the Si-Ge-Sn class of materials, including all alloys mentioned in this section, constitutes a new paradigm in the integration of Si based electronics with optical components on a single chip. In fact, all fabrication techniques needed for new group IV alloys, are perfectly compatible with CMOS standard processes and facilities.

2.1.1 Fabrication tolerances

Slot waveguides and PWEF sensors presented until now, have been represented assuming an ideal geometry. In fact, vertical sidewalls (Fig. 4 a-b, Fig. 6, Fig. 8 a-b) are very difficult to be obtained by the state-of-the-art etching processes (e.g., inductively coupled plasma, ICP). Thus, deviations from ideal case have to be considered and one of the most important parameters quantifying this effect is the tilting angle θ, as shown in Fig. 9. By this way, it is possible to distinguish between vertical (θ=0°) and non vertical (θ≠0°) sidewalls.

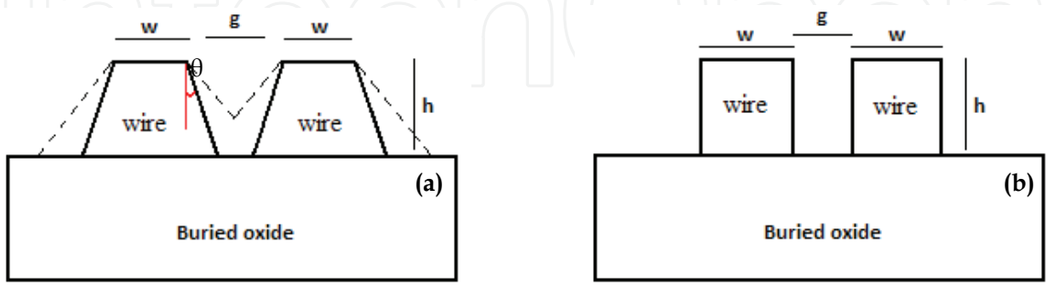

Fig. 9. Schematic view of slot waveguide. (a) real non vertical architecture for theoretical analysis of fabrication tolerances; (b) ideal slot waveguide with vertical sidewalls.

All well known performance parameters (S_h, Γ_C, Γ_S) have to be evaluated for different tilting angles θ° in the range 0°-10°. To this purpose, interesting results have been plotted in Fig. 10.

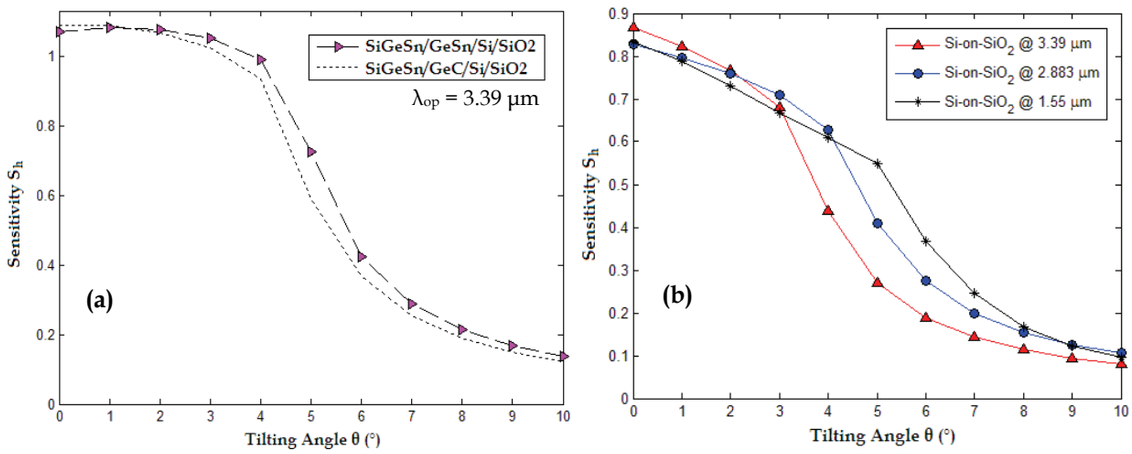

Fig. 10. Sensitivity of optimized slot waveguides as a function of the tilting angle θ with slot region width g fixed at 100nm in all cases. (a) Tolerance analysis of group IV-based optimized slot waveguides presented in Fig. 8; (b) Tolerances analysis of conventional SOI slot waveguides (@ 1.55μm, w = 230nm, h = 500nm, @ 3.39 & 2.883 μm, see also Fig. 7b).

All sensitivity values corresponding to θ = 0°, are referred to optimized slot waveguides characterized by vertical sidewalls. By observing Fig. 10a and 10b, it is evident that the greater the tilting angle, the lower the sensitivity. This effect is justified by the fact that increasing values of θ will produce a reduction of the slot region volume. Moreover, the slot region width g is not constant along y-direction. In conclusion, for θ > 4°, the slot mode cannot propagate because the optical field confinement in the slot region approaches zero.

Fabrication tolerance analysis represents an important aspect to estimate the real sensor performance. By this way, the solution to the technological problems presented above, is strictly related to the optimization of the etching process for a given combination of material systems. However, standard etching processes can assure tilting angles within 1°-2°. Generally, slot waveguides designed to operate in mid-IR wavelength range, exhibit greater tolerance margins because of their relaxed dimensions (Fig. 10a). To this purpose, θ < 3°-4° represents a good trade-off between technological constraints and device performance.

2.1.2 State of the art of slot waveguides designed for chemical sensing

All theoretical and experimental results demonstrate that slot waveguides are the best suitable photonic devices for sensing applications. In fact, if properly designed, they allow to concentrate a high optical field percentage in the cover medium, improving the interaction between the optical field and the chemical process, thus the limit of detection.

To this purpose, alternative solutions have been proposed in literature with the aim to enhance the efficiency and performance of photonic chemical sensors. For example, slot waveguides based on polymeric materials can ensure high performance, although characterized by low refractive index contrast Δn (Bettotti et al., 2011). In addition, multiple-slot waveguides represent an intriguing solution. By using multiple slot waveguides such as those presented in Fig. 11a-b-c, it is possible to significantly increase the sensitivity for both homogeneous ($\Delta n_{eff}/n_c \sim 0.2$) and surface sensing ($\Delta n_{eff}/\Delta\rho \sim 10^{-4}$ RIU/nm) (Kargar & Lee, 2009; Sun et al. 2009).

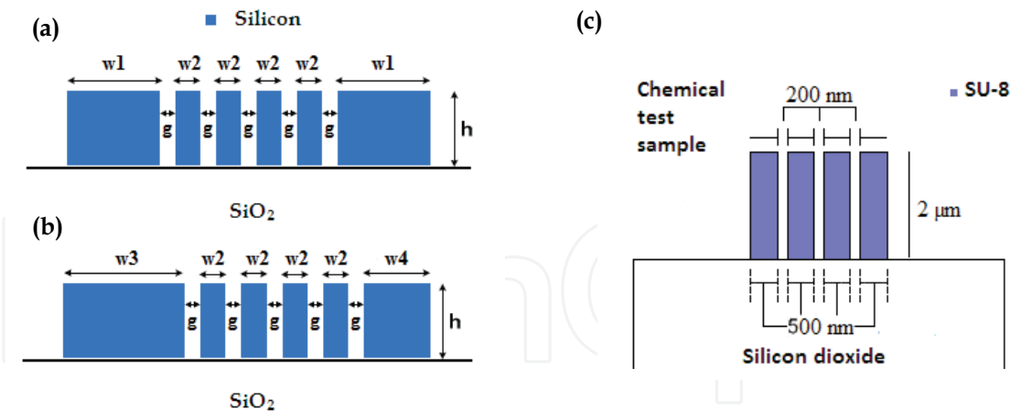

Fig. 11. Cross section of a symmetric (w1 = 133nm, w2 = 33nm, g = 20nm, h = 250nm) (a), and asymmetric (w3 = 200nm, w2 = 33nm, g = 20nm, w4 = 67nm, h = 250nm) (b), silicon quintuple-slot waveguides. Cross section of SU-8 (n_{SU-8} = 1.565 @ 1.55µm) multiple slot waveguide (c).

This improvement is justified by the fact that, in multiple-slot waveguides, the interaction between the optical field and the chemical test sample can be distributed in a larger area, in comparison to single slot waveguides. However, technological problems and reduced mode excitation usually limit the practical number of slots to three.

Another slot waveguide architecture evolution is represented by horizontal slot waveguide, as sketched in Fig. 12a. By this way, the optical propagating slot mode is quasi-TM, because the E_y-field is the only E-field component that undergoes discontinuities.

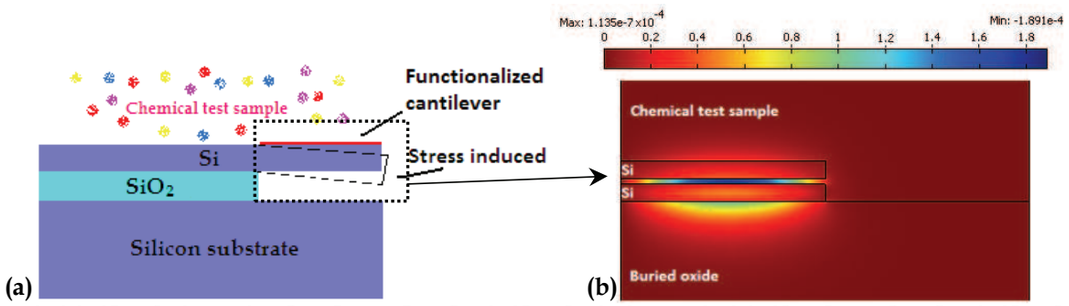

Fig. 12. Cross sectional view of the horizontal slot chemical sensor (a) with the spatial distribution of the fundamental TM optical mode (b).

A vertical slot fabrication can be realized by ICP etching, for example. However, etching in a very narrow region (slot region width g ~ 20-100nm) can produce large roughness in the vertical interface. By this way, in vertical slot waveguides, where the E_x-field is concentrated at the interface between the high and low refractive index region, propagation losses can be very high, such as 11.6 ± 3.6 dB/cm in a single slot of 50nm (Baehr-Jones et al., 2005). This problem can be partially solved by using horizontal slot waveguides (Fig. 12a-b). In fact, the latter can be fabricated by using thermal oxidation or deposition of different layers. By this way, the quasi TM-mode is not affected by surface roughness and propagation losses can be significantly reduced, down to 6.3 ± 0.2 dB/cm, 7.0 ± 0.2 dB/cm for a single and multiple slot waveguides, respectively (Sun et al., 2007). In Fig. 12a it is possible to see how the adsorption of target molecules on the cantilever surface, causes a small variation in the position of the

functionalized cantilever. Consequently, an effective index change Δn_{eff} is caused by strain optic effect. Normally, the stress induced by proteins lies in a range between 3000 and 15000 με (ε is the strain induced on the cantilever). Thus, the sensor response and the sensitivity are quite high. On the contrary, there are some aspects that limit the mass-scale production of these particular photonic sensors. First of all, the mechanical deformation, directly responsible of the sensing principle described above, has to be ensured also by very accurate technological steps, strongly influencing the sensor lifetime. Another important limitation concerns with the reliability of the sensing procedure. In fact, if the cantilever is corrupted by other molecules or particles not involved in the sensing detection, the calibration of the same sensor could be wrong, thus procedure has to be repeated more than one time.

In conclusion, both vertical and horizontal slot waveguides represent very promising photonic devices for chemical sensing applications. The high refractive index contrast between silicon and its oxide provides excellent optical confinement. By this way, it is possible to guide high optical intensity in the cover medium, preventing non linear effects in silicon, such as two-photon absorption (TPA), that can lead to high optical losses.

3. Advanced platforms for chemical photonic sensing

Generally, the choice of the photonic device suitable for label-free sensing applications (rib waveguide, photonic wire and slot waveguide) concerns with the possibility to ensure the best overlapping between optical field and chemical/biochemical sample. As analyzed until now, in both homogeneous and surface sensing the optical transduction leads to the effective index change Δn_{eff}. However, this optical variable has to be transformed into an analytically useful signal. To this purpose, several photonic integrated platforms have been proposed in literature. In particular, it is possible to distinguish between two different types of optical readout: the intensity and wavelength readout (power and wavelength interrogation, respectively). For example, photonic chemical sensors based on optical absorption are characterized by an intrinsic intensity readout, because the change of the absorption coefficient α is directly linked to the output optical intensity, according to the Beer-Lambert law. By this way, it is possible to register the chemical-to-optical transduction by using a photodiode as a transducer (Fig. 1).

In this context, advanced optical platforms for chemical sensing will be investigated in this Section.

3.1 Mach-Zehnder interferometer

The operation principle of the integrated Mach-Zehnder interferometer (MZI) is illustrated in Fig. 13a. Light is introduced through a photonic waveguide (e.g., slot waveguide) in the Y-branch on the scheme left side. By this way, the input optical power I_{IN} is split into two optical beams with an half power $I_{IN}/2$ in the upper and lower arms, called "sensing" and "reference" arm, respectively. If any optical phase delay is applied to the guided mode in the sensing arm ($\Delta\varphi = 0$), light will be combined at the output Y-branch exhibiting an output optical power $I_{OUT} = I_{IN}$. In all different cases ($\Delta\varphi \neq 0$ in sensing arm), the optical output power will be different from the input one ($I_{OUT} \neq I_{IN}$), according to Eq. 9.

$$I_{OUT} = I_{IN}\cos^2\left(\frac{\Delta\varphi}{2}\right) = I_{IN}\cos^2\left(\frac{\pi\Delta n_{eff}L}{\lambda}\right) \tag{9}$$

In Eq. 9, L is the interaction length, thus the guiding path in which the overlapping between the optical field and the chemical test sample occurs, and λ is the operative wavelength.

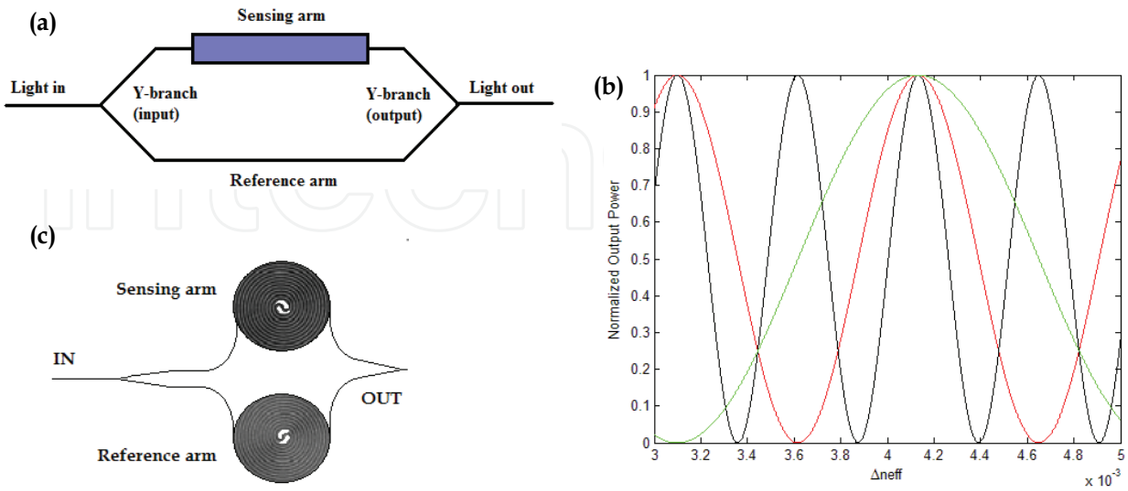

Fig. 13. (a) Schematic view of Mach-Zehnder interferometer; (b) Normalized output power as a function of different values of L (black = 3mm, red = 1.5mm, green = 750nm, λ_{op} = 1.55μm); (c) Image of a balanced MZI characterized by spiral arms.

In Fig. 13b, it is possible to see the effect of different values of L on sensing efficiency. In fact, sensor resolution is the capability to detect the minimum effective index perturbation. By this way, it is possible to conclude that the longer the interaction length, the higher the sensor resolution. Graphically, this concept can be observed by analyzing the steepness and width of each $\cos^2$ lobe. In conclusion, the closer the transmission spectra lobes, the smaller the detectable effective index change. Obviously, it is not convenient to realize cm-long arms because photonic chemical sensors have to be characterized by very small footprints. To this purpose, interesting technological solutions have been presented in literature. In Fig. 13c, a spiral path configuration is presented. By this way, it is possible to improve sensor performance and efficiency, without compromising the sensor dimensions. In fact, mm-long arms (~ 2-3mm) can be realized and concentrated in spiral architecture characterized by μm-long diameter.

Very high integration with spiral-path configurations allows to design biosensor arrays for multiplexed real-time and label-free molecular detection. Ultra high performance can be achieved in terms of sensitivity and LOD. For example, the measured sensitivity of the 2.1 mm-long interferometer fabricated on SOI wafer with 2μm silica under 260nm of silicon, is $d\varphi/dn_C$ = 4930 rad/RIU, while the calculated change of polydimethylsiloxane (PDMS) refractive index upon xylene is 8.7×10^{-7} RIU/ppm (Saunders et al., 2010). PDMS has been used as sensor cladding in order to enable sensing of BTEX (Benzene, Toluene, Ethylbenzene, Xylenes) volatile organic compound. In addition, a surface mass coverage of 0.3 pg/mm^2 can be detected with a silicon photonic wire MZI sensor array, with integrated SU-8 micro-fluidic channel (Densmore et al., 2009). In conclusion, the principal penalty of using MZI photonic sensors is represented by the cosine-dependent intensity function.

In fact, the signal change is not easily resolvable near the maximum and minimum of the cosine function.

3.2 Surface plasmon resonance biosensors

A surface plasmon is a localized electromagnetic wave that propagates along the metal-dielectric interface and exponentially decays into both media. Surface plasmons can be excited due to the resonant transfer of the incident photon energy and momentum to collectively oscillating electrons in a noble metal. The plasmon resonance condition is given by the following expression (Jha, R. & Sharma, 2010):

$$k_0 n_C \sin(\theta) = k_0 \left(\frac{\varepsilon_{mr} n_S^2}{\varepsilon_{mr} + n_S^2} \right)^{\frac{1}{2}} \tag{10}$$

In Eq. 10, ε_{mr} is the real part of the metal dielectric function, n_C is the refractive index of light coupling glass, n_S is the refractive index of sensing medium (dielectric), λ is the wavelength of incident light and k_0 is the wave number ($2\pi/\lambda$). The resonance condition is satisfied when β (propagation constant of the light beam coupled at the angle θ) is equal to β_{SPW} (propagation constant of the surface plasmon polariton). The resonant condition is expressed by Eq. 10 when $\theta = \theta_{SPR}$. At the resonant condition, the reflected light intensity encounters a sharp dip due to optical absorption by surface plasmon wave (SPW). This dip can be easily detected by the photo-detector, as reported in the scheme proposed in Fig. 14.

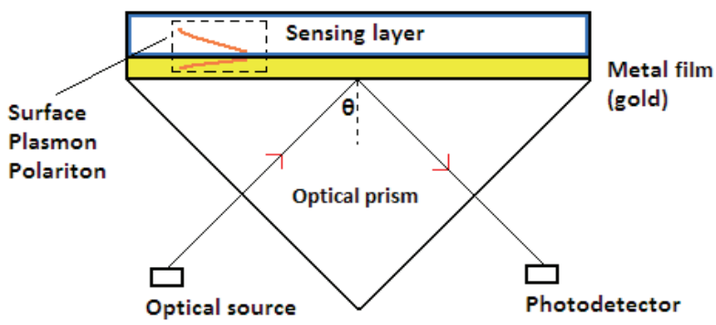

Fig. 14. Schematic view of a SPR biosensor characterized by prism coupling configuration.

Bio-molecular recognition elements at the metal surface selectively capture target analytes in a chemical liquid test sample, the reflectance dip makes a shift due to the change of local refractive index near the surface. In particular, plasmonic related sensing procedure has been used for label-free detection of biological analytes at pico/femto-molar level, pesticides, immunoassays, DNA with a refractive index resolution of 1.4×10^{-7} (Le et al. 2011), RNA, allergens and human blood-group identification (Jha & Sharma, 2010). For example, a SPR mid-infrared immunosensor used in a Fourier-transform infrared (FTIR) spectroscopy platform, exhibits a sensitivity of 3022 nm/RIU and a limit of detection of ~70 pg/mm^2 (DiPippo et al., 2010). Generally, the detection of the SPR change due to the adsorption of target molecules on the sensing surface, can be quantified by monitoring the resonant intensity, wavelength or angle change. Although SPR chemical sensors exhibit high sensing performance, they are characterized by some operative constrains. In particular,

surface plasmon evanescent field penetrates in the sensing layer only for ~100nm. In this way, it is not possible to detect large target molecules like cells and bacteria. Another limitation concerns with the impossibility of the SPR photonic sensor, to distinguish between the refractive index surface change and the bulk solution refractive index change. Then, if the sensor is covered by a complex chemical solution (e.g., blood, bacteria-solution), it is very difficult to ensure high detection resolution. To this purpose, interesting architectures have been proposed in literature such as a novel optical structure, in which the metal layer is sandwiched by two dielectric layers with similar refractive index. In this way, both long (LSPR) and short (SSPR) surface plasmon modes can be generated at both metal-dielectric interfaces, allowing to differentiate the background and surface bound refractive index change (Li et al., 2010). In conclusion, all commercialized SPR biosensors can be characterized by different coupling methods. In addition to prism coupling configuration sketched in Fig. 14, there are guided-wave, fiber optic and grating coupling configurations (Marrocco et al., 2010). Slot plasmonic waveguides have been also proposed as an integrated chemical sensor with high sensitivity (Hu et al., 2010).

3.3 Chemical sensors based on photonic crystals

Photonic crystals (PhCs) are periodic systems characterized by symmetrical separation between high dielectric and low dielectric regions. Generally, it is possible to distinguish between three different geometrical configurations as a function of the spatial periodicity. In fact, there are one-dimensional PhCs where the dielectric function periodicity is distributed only to one dimension (1D), thus bi-dimensional (2D) and three-dimensional (3D) PhCs. By using photonic crystals it is possible to guide and trap the light. In addition, photonic crystals exhibit a very large selective photonic band gap that prevents photons in the band gap from propagating in the material. By this way, it is possible to design a photonic waveguide by creating a line defect in the structure. The basic element of a photonic crystal is called “elemental” or “primary cell” and it can be represented by a line, circle, hexagonal or tetrahedral geometry, to name a few. For example, the periodical repetition of the hexagonal geometry produces a photonic crystal with a particular structure defined as “honeycomb”. Photonic crystals exhibit interesting and promising features, suitable for high performance chemical sensing.

3.3.1 Integrated optical Bragg-grating-based chemical sensors

Photonic Bragg gratings are characterized by a periodic spatial distribution of the dielectric constant, thus of the refractive index, along the propagation direction. Consequently they are photonic crystals and exhibit a selective range of propagating wavelengths.

It is possible to realize an integrated optical sensor based on Bragg gratings in SOI technology, as sketched in Fig. 15 (Passaro et al., 2008). A Bragg grating is characterized by a periodic perturbation of the waveguide refractive index along the propagating direction z:

$$n(x,y,z) = n_0(x,y) + \Delta n(x,y,z) \tag{11}$$

In particular, $n_0(x,y)$ is the waveguide refractive index distribution, $\Delta n(x,y,z)$ represents the periodic refractive index change characterized by a period Λ (Fig. 15a). Λ represents a physical parameter that has to be designed in order to ensure a precise center wavelength of

the Bragg grating spectral response (Fig. 15b), following the relation as in Eq. 12. In particular, m is the grating order, n_{eff} is the effective index of the propagating mode and λ_C is the central wavelength, previously defined.

$$\Lambda = \frac{m}{2n_{eff}}\lambda_C \tag{12}$$

In conclusion, the grating reflectivity can be expressed by the following expression:

$$R(\delta) = \frac{|k|^2 \tanh^2(\gamma L)}{\gamma^2 + \delta^2 \tanh^2(\gamma L)} \tag{13}$$

where k is the coupling coefficient between backward and forward propagating optical modes, L is the grating length, γ and δ are two optical parameters defined as:

$$\delta = \frac{2\pi}{\lambda} n_{eff} - \frac{\pi}{\Lambda} \;;\; \gamma = \sqrt{|k|^2 - \delta^2} \tag{14}$$

By this way, it is possible to explain the sensor device operative regime. In particular, all geometrical parameters (h, H, D, W, d, Λ) and the index contrast Δn, have to be designed in order to determinate the central operative wavelength λ_C. In Fig. 15b, it corresponds to 1550 nm. By observing Eq. 12, it is possible to see that λ_C only depends on the effective index of the mode propagating, because the grating period Λ is fixed after the device fabrication. Consequently, any effective index change Δn_{eff} induced by homogeneous or surface sensing, causes a central wavelength shift, $\Delta\lambda_C$.

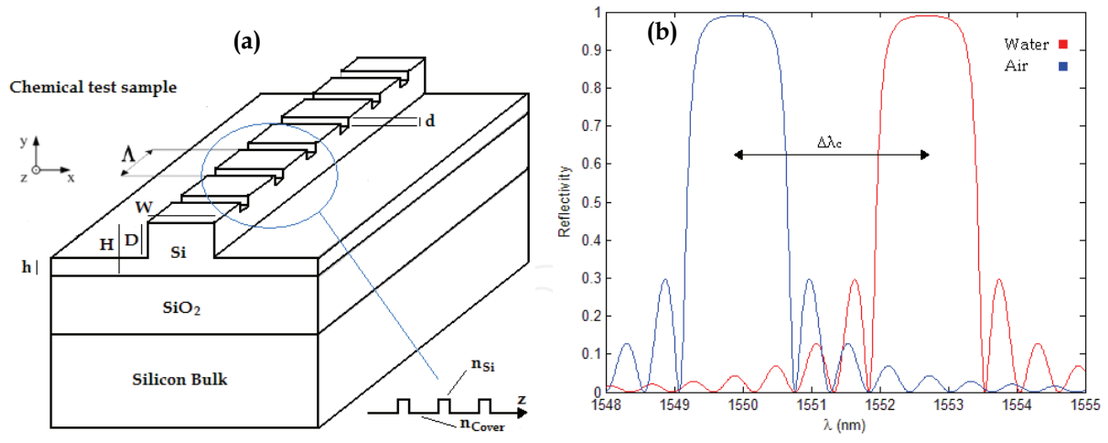

Fig. 15. (a) Schematic view of a grating–based sensor device. (b) Spectral response of the first-order grating for different values of cover refractive index (H = 1μm, d = 30nm, W = 0.56μm, D = 0.62μm, Λ = 240nm, n_{air} = 1, n_{water} = 1.33).

In the graph reported in Fig. 15b, the sensor operative regime is characterized by λ_C = 1550nm with air cover. When the sensor is exposed to aqueous solution (e.g., water), λ_C = 1552.7nm. By this way, if the selected operative wavelength λ_{op} is 1550nm, than it is possible to detect a change in the solution composition by measuring the new center wavelength shift, $\Delta\lambda_C$ = 2.69nm. By using third-order grating based sensor devices (m = 3), it

is possible to maximize the device efficiency and employ shorter length chips. In conclusion, grating sensitivity can be defined as following:

$$S = \frac{\partial \lambda_C}{\partial n_{clad}} = \frac{\partial \lambda_C}{\partial n_{eff}} \frac{\partial n_{eff}}{\partial n_{clad}} = \frac{\Lambda}{m} S_w = \frac{\lambda_C}{2n_{eff}} S_w \tag{15}$$

In Eq. 15, n_{clad} is the cladding refractive index and S_w is the waveguide sensitivity, whose definition depends on sensing mechanism (homogeneous or surface sensing). A device sensitivity S around 120nm/RIU is practically obtainable. In conclusion, Bragg gratings analyzed above can be adopted in different waveguide architectures such fiber optics (fiber Bragg gratings, FBG). Sensitivity of 92 nm/RIU has been demonstrated for refractive index change of water in a FBG chemical sensor (Lee et al., 2010).

The sensing principle described above is based on the wavelength interrogation of the Bragg grating. However, another type of interrogation can be used, based on the incident angle θ (°) that the propagating light forms with the Bragg grating surface. The device operation can be expressed by the following relation:

$$m\lambda = 2\Lambda \sin\theta \tag{16}$$

Coupling wavelength λ depends on the grating period and interrogation angle. By this way, by monitoring changes in coupling angle, molecular binding at the waveguide surface can be detected and measured by using SPR sensors, as in Fig 16a-b. In particular, the reflected intensity spectrum exhibits a sharp resonance peak at the coupling wavelength.

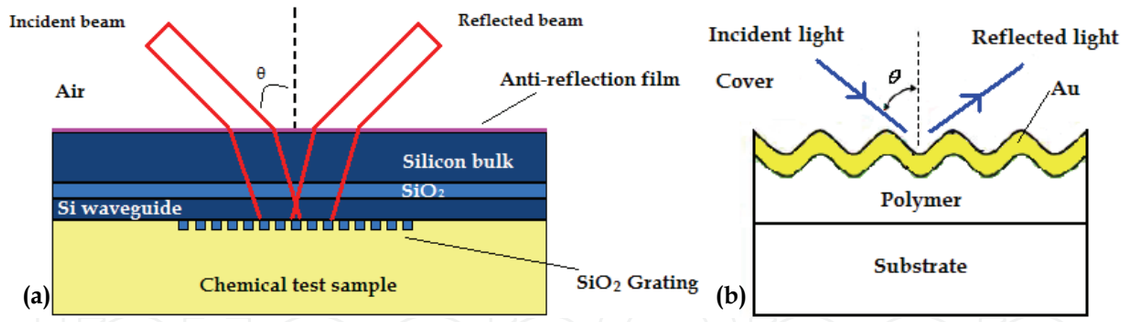

Fig. 16. (a) Schematic view of a photonic silicon waveguide sensor based on surface grating interrogation. (b) Chemical grating–coupled surface plasmon resonance sensor.

The sensing principle based on angle interrogation can be used also in surface plasmon resonance sensor characterized by a grating coupling. In particular, a refractive index resolution of 1.5×10^{-6} RIU has been demonstrated by using a sensor as that sketched in Fig. 16b (Kuo & Chang, 2010).

3.3.2 State of the art of integrated chemical sensors based on photonic crystals

Nowadays, one and two dimensional photonic crystals represent an interesting and promising research field for sensing applications, because of their compactness and high resolution in the detection process. Recently, a photonic crystal slot waveguide has been fabricated and used as infrared (IR) absorption spectrometer for methane monitoring. The

principle of IR absorption spectroscopy is based on the Beer-Lambert law, described in the previous section (Lai et al., 2011).

The photonic device shown in Fig. 17a, has been realized by using a circular geometry as primary cell.

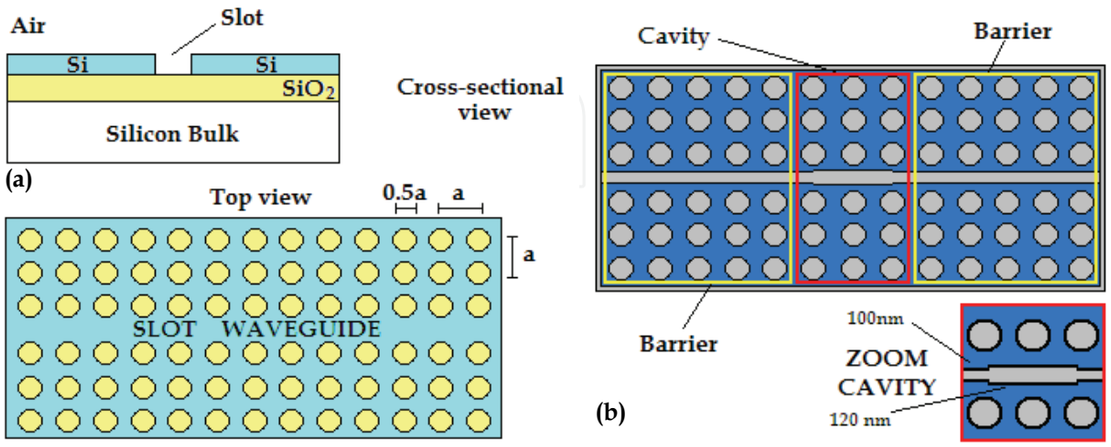

Fig. 17. (a) Photonic crystal slot waveguide built on SOI platform. (b) Photonic crystal resonant cavity based on slot waveguide for sensing application.

Consequently, a periodic 3D spatial distribution of the refractive index is realized with a lattice constant a. In fact, it is possible to observe that circular holes are characterized by low refractive index (n_{SiO2}), while the reciprocal space represents the high refractive index region (n_{Si}). A slot waveguide has been realized by introducing a line defect. By this way, a high electric field intensity is localized in a low-index (n_{air}) 90nm wide slot. The silicon photonic crystal slot waveguide device is characterized by a total length of 300μm in order to increase the optical absorption path length. A methane concentration of 100ppm in nitrogen has been measured.

In Fig. 17b a photonic crystal air-slot cavity has been presented (Jagerska et al., 2010). The structure is similar to the previously analyzed slot waveguide. In fact, the proposed air-slot cavity has been processed on a 220nm thick silicon-on-insulator wafer with a 2μm buried oxide layer. The cavity has been realized by reducing the line defect width by 20nm, thus unchanging the photonic crystal lattice constant. Reduced-slit width results in the formation of reflective barriers for the cavity mode. By this way, only resonant wavelengths can propagate inside the photonic cavity. The sensor has been tested by exposing the chip to gases of different refractive index such as N_2 (RI = 1.00270), He (1.00032) and CO_2 (1.00407) at the operative wavelength, λ_{op} = 1570nm. The refractive index change (Δn) due to the sensor exposition to different gases, causes a resonant wavelength shift (Δλ). Consequently, it is possible to detect different gas concentrations by monitoring the cavity transmission spectrum.

The sensor sensitivity can be defined as follows:

$$S = \frac{\Delta\lambda}{\Delta n} = \Gamma \frac{\lambda}{n_{eff}} \tag{17}$$

In Eq. 17, λ is the resonance wavelength of the cavity, Γ is the mode field overlap and n_{eff} the modal effective index. The high quality factor of the cavity (Q ~ 2.6×10^4) allows to achieve an experimental sensitivity S = 510 nm/RIU and a detection limit below 1×10^{-5} RIU.

In conclusion, other intriguing solutions have been proposed such as a single-defect silicon 2D photonic crystal nano-cavity for strain sensing (Tung et al., 2011). The sensing principle is the same as the gas sensor described above, but the resonant wavelength shift is induced by geometrical longitudinal and transverse strain. The theoretical minimum detectable strain for the photonic crystal cavity has been estimated to be 8.5×10^{-9} ε (8.5nε). By this way, advanced chemical sensing applications can be contemplated, based on cantilever sensing architectures.

3.4 Integrated optical directional coupler biosensors

The use of optical directional couplers for the measurement of interactions between biological molecules and the detection of target chemical and biochemical species, is an interesting research field for sensing applications. In fact, these photonic sensors are characterized by high performance and real-time monitoring of multiple outputs. The scheme of a directional coupler is presented in Fig. 18.

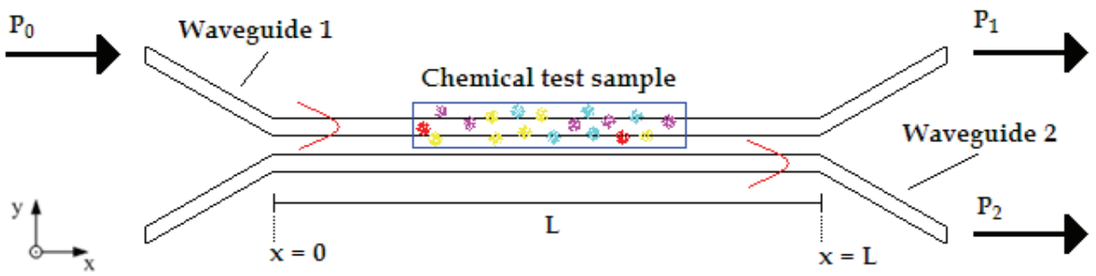

Fig. 18. Schematic representation of an integrated direction coupler.

The sensing principle is based on the super-mode theory. In Fig. 18 it is possible to see that only one waveguide (in this case the waveguide 1), is directly exposed to the chemical test sample. The other one has to be isolated by using appropriate coatings (e.g., polymers, Teflon). Generally, both waveguides have to be designed as symmetrical (e.g., identical geometries and contrast index Δn), in order to exhibit the same propagation features. In this way, β_1 and β_2, the propagation constants of the optical modes propagating in the waveguide 1 and 2, respectively, can be considered equal ($\beta_1 = \beta_2$) in a "synchronous" regime, where the propagation constant mismatch is equal to zero ($\Delta\beta = 0$). By assuming that an optical power P_0 is introduced in the waveguide 1 at the section x = 0, optical powers (P_1, P_2) at the output section (x = L) can be calculated by the following expressions:

$$P_2 = \frac{\sin^2\left\{\left[(kL)^2 + \left(\frac{\Delta\beta L}{2}\right)^2\right]\right\}^{\frac{1}{2}}}{1+\left(\frac{\Delta\beta}{2k}\right)^2} P_0 \,,\; P_1 = P_0 - P_2 \tag{18}$$

where k is the coupling coefficient and depends on the overlap between the two propagating modal fields, and L is the device length. In synchronism condition ($\Delta\beta$ = 0), complete power transfer from the waveguide 1 to the waveguide 2 is achieved when kL = π/2, 3π/2, 5π/2, etc. In this way, it will results $P_2 = P_0$ and $P_1 = 0$, at the end section x = L.

When a chemical test sample, gas or liquid solution, covers the waveguide 1, the refractive index of the cover medium will change, causing a modal effective index change of the propagating mode n_{eff1}. Consequently, the synchronous coupling condition will not be ensured because $\beta_1 \neq \beta_2$, thus $\Delta\beta \neq 0$. According to Eq. 18, P_1 will be different to zero because a complete optical power transfer now cannot occur. By monitoring the change of coupler outputs P_1 and P_2, it is possible to detect a particular chemical target and estimate its concentration with high limit of detection. The sensitivity S can be calculated as follows:

$$S = n_{clad(REF)} \left. \frac{\partial T}{\partial n_{clad}} \right|_{nclad=nclad(REF)} \tag{19}$$

where T is the transmittance registered at the output of the reference waveguides, n_{clad} is the chemical analyte refractive index and $n_{clad(REF)}$ is the reference analyte refractive index value for which the derivative is calculated. The highest sensitivity can be achieved at the point of maximum slope of the main peak of the transmittance curve. Consequently, this condition indicates the operating point of the sensor. Obviously, the overall sensitivity depends on the waveguide sensitivity, S_W. In this context, the use of slot waveguides represents the best solution. To this purpose, interesting results have been obtained by using coupled slot SOI waveguides sketched in Fig. 19a. In particular, a sensitivity S = 215.29 was achieved for quasi-TE mode with a coupler length L = 400μm (Passaro et al., 2009b).

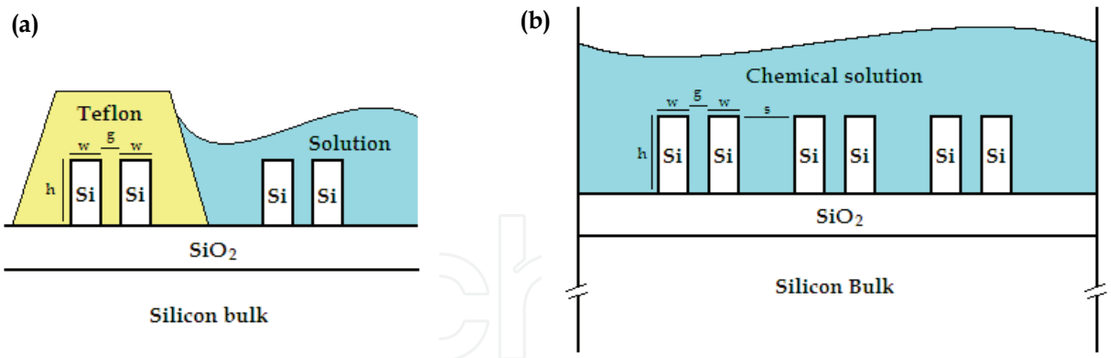

Fig. 19. (a) Architecture of coupled SOI slot waveguides for chemical sensing (h = 324nm, w = 180nm, g = 100nm). (b) Multi-channel directional coupler with slot waveguides (h = 300nm, w = 180nm, g = 100nm, s = 500nm).

The sensor sketched in Fig. 19a allows to estimate an analyte concentration in the aqueous solution. In particular, the photonic sensor integrated with a footprint of ~ 1mm², can detect a minimum refractive index change of ~10^{-5} and it can be adopted to estimate the glucose concentration in aqueous solution with a theoretical resolution of 0.1 g/L.

In Fig. 19b, a multi-channel directional coupler with slot waveguides is shown (McCosker & Town, 2010a). The sensing principle adopted in this device is different with respect to the

previous one. In particular, it is possible to observe that there is not an isolated waveguide, because all silicon rails are simultaneously covered with the chemical solution. In this way, it is impossible to register a propagation constant mismatch change, because it will be constant. Thus, the sensing principle consists in the coupling coefficient change Δk, as a function of the cover refractive index change Δn_{clad}. In particular, the coupling coefficient k has an exponential dependence on analyte refractive index (McCosker & Town, 2010b). Interesting results have been theoretically demonstrated with a 1,607μm-long device. For example, a concentration of glucose or ethanole dispersed in deionised water could be detected with sensitivities of -172 (negative T slope in Eq.19) and +155 (positive T slope), respectively.

Photonic sensors based on directional couplers, exhibit very high performance. However, it is necessary to achieve a good trade-off between sensitivity and device length. In fact, in both sensing principles as analyzed above, mm-long interaction lengths allow to appreciate transmittance changes at the device output.

3.5 Chemical sensors based on integrated optical resonant microcavities

Photonic devices exhibiting best performance for chemical sensing are those based on resonant microcavities (Passaro et al., 2007b). In fact, they allow to achieve ultra low detection limits and ultra high sensitivities due to their wavelength interrogation, poorly influenced by optical noise. Optical resonant microcavities can be designed with different paths, for example ring, race-track or spiral-path ring. Generally, a resonance structure consists in a waveguide closed into a loop and coupled with one or two input/output bus waveguides (Fig. 20a). Resonance theory imposes the propagation of precise guided stationary modes inside the resonance cavity, in particular those modes whose wavelengths satisfy the well known resonance condition:

$$\lambda = \frac{2\pi n_{eff} R}{m} \tag{20}$$

where n_{eff} is the modal effective index, R is the ring resonator radius and m is an integer (m = 1, 2, 3,…, n), that represents the resonant order. This result has been obtained by imposing that the total round trip shift of the guided mode inside the ring resonator, must be an integer multiple of 2π. The analytical expression of the transmission spectrum of a ring resonator with a single bus (Fig. 20a), is given by the following equation:

$$T_{ring}(\lambda) = \frac{\alpha^2 + t^2 - 2\alpha t \cos\left(\frac{2\pi L n_{eff}}{\lambda}\right)}{1 + \alpha^2 t^2 - 2\alpha t \cos\left(\frac{2\pi L n_{eff}}{\lambda}\right)} \tag{21}$$

In Eq. 21, α is the loss factor that gives the field attenuation after one round trip through the ring cavity waveguide (i.e., α = 1 in lossless case). The cosine argument represents the round trip phase, $L = 2\pi R$ is the cavity length depending on the ring radius, and t is the coupling ratio between the bus waveguide and the ring cavity.

In this context, the sensing principle consists in a resonant wavelength shift $\Delta\lambda$ due to the modal effective index change Δn_{eff} caused by the presence of the chemical analyte in the sensing area (Fig. 20b).

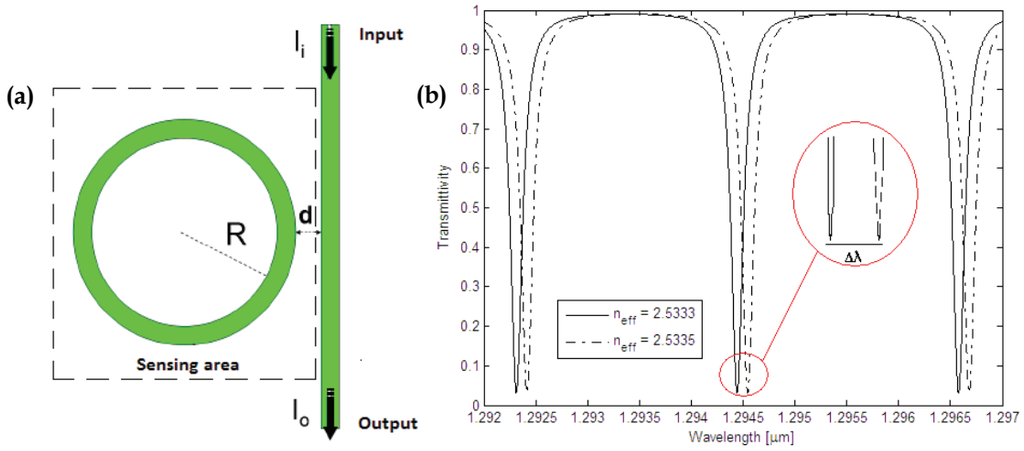

Fig. 20. (a) Schematic top view diagram of a silicon photonic ring resonator with a single bus waveguide. (b) Transmission spectrum of the ring resonator before (n_{eff} = 2.5333) and after (n_{eff} = 2.5335) the exposure to the chemical analyte.

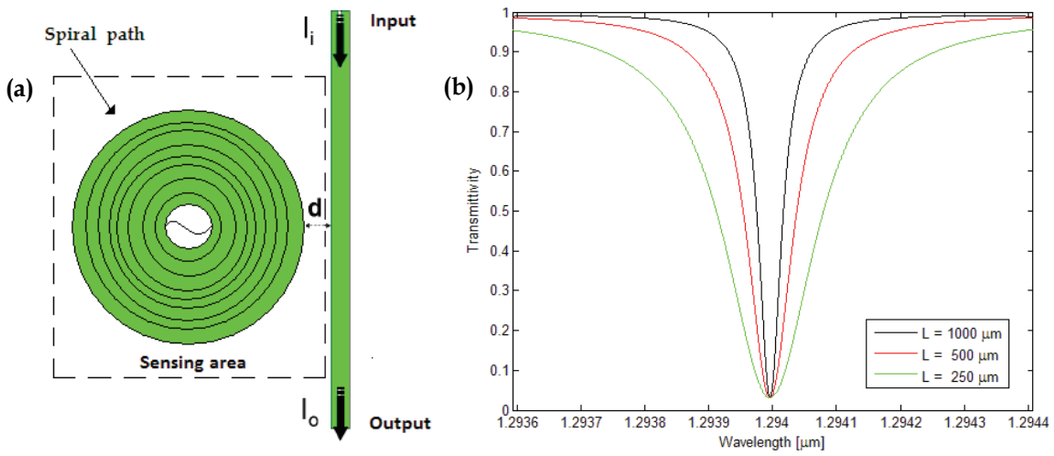

Fig. 21. (a) Top view of the spiral-path folded resonant cavity coupled to a bus waveguide. (b) Parametric analysis of the transmission spectrum (Lorentzian), windowed to a single resonant wavelength (λ_{op} = 1.294μm), as a function of three different interaction lengths.

The transmission spectrum shown in Fig. 20b has been calculated for a 250μm-long cavity characterized by α = 0.8875, t = 0.9198. In particular, it is possible to appreciate that a modal effective index change $\Delta n \sim 10^{-4}$ theoretically induces a resonant wavelength shift Δλ of about 0.1nm. As analyzed about the MZI configuration (see. Para. 3.1), in chemical sensors based on single ring resonator as sketched in Fig. 20a, the resonant cavity length assumes a key role in the photonic sensor optimization. In fact, in Fig. 21b it is possible to see that the longer the interaction length "L" between the optical field and the chemical analyte, the higher the detectable resolution.

The most important parameter that allows to appreciate the ring-based sensor resolution is the linewidth of its transmission spectrum. In fact, in Fig. 21b it is possible to see that the longer the interaction length, the sharper the resonant peak. By this way, it is possible to see that a small linewidth corresponds to a high slope of the resonant peak, resulting in a signal

change easily resolvable near the maximum and minimum of the transmission function. However, very long interaction lengths will result in large device areas that are not suitable for high scale integration. To this purpose, intriguing folded spiral–path cavities have been proposed (Fig. 21a). In fact, they allow to achieve mm-long interaction length concentrated in very small footprint (~μm²). The sharpness of the resonant peak in a ring resonator transmission spectrum is usually expressed in terms of its quality factor Q:

$$Q = \frac{\lambda}{\Delta\lambda_{FWHM}} = \frac{\pi n_g L}{\lambda}\left[\arccos\left(\frac{2\alpha t}{1+\alpha^2 t^2}\right)\right]^{-1} \quad (22)$$

In Eq. 22, λ is the resonant wavelength, $\Delta\lambda_{FWHM}$ is the resonance full-width-at-half-maximum (*FWHM*) and n_g is the ring resonator group index. It is evident that the smaller the linewidth, the higher the resonant cavity quality factor.

In conclusion, it is possible to revisit the concept of sensitivity and limit of detection (LOD):

$$S = S_W \frac{\lambda}{n_{eff}}, LOD = \frac{\Delta\lambda}{S} \quad (23)$$

The sensitivity *S* (nm/RIU) depends on the waveguide sensitivity S_W and other well known parameters (resonant operative wavelength λ and modal effective index n_{eff}). The limit of detection *LOD* (RIU), depends on the minimum detectable resonant wavelength shift Δλ. By this way, ultra high performance for chemical, biochemical and gas sensing (*S* ~ 2000 nm/RIU, *LOD* ~ 3.8×10^{-5} RIU) can be achieved by using slot waveguides (Passaro et al., 2011).

Particular research efforts are still doing today in this field. In fact, the state-of-the-art of photonic sensors for bio-sensing applications is mainly dedicated to the optimization and characterization of novel resonant microcavities based on slot waveguides. In particular, a novel integrated SOI optic racetrack resonator has been proposed for bio-sensing applications (Malathi et al., 2010). The device is capable of distinguishing compressive and tensile stresses on a cantilever due to conformational changes of protein, Bovine Serum Albumin (BSA) and Immunoglobulin G (IgG). The change of surface stress upon adsorption of IgG is compressive, while for BSA it is tensile. The sensing principle of this specific photonic sensor configuration can be expressed by the following equation:

$$\frac{\Delta\lambda}{\lambda} = \frac{\Delta L}{L} + \frac{\Delta n_{eff}}{n_{eff}} \quad (24)$$

When the bio-molecules adhere to the device surface, both effective refractive index and racetrack length change due to photo elastic effect. When the cantilever bends, one arm of the racetrack experiences a small variation in *L* by Δ*L* and n_{eff} changes by Δn_{eff}, due to the strain optic effect. Bio-molecules stress on the cantilever has been simulated and the wavelength shift from the resonance has been found to be 0.3196×10^3 nm/με, where ε is the strain induced on the cantilever. Normally, the stress induced by proteins lies in a range between 3000με and 15000με, thus the sensor response and sensitivity obtained are quite high.

In this context, an ultrasensitive nano-mechanical photonic sensor based on horizontal slot waveguide resonator, has been also proposed on SOI platform (Barrios, 2006). The effective

index variation can be read out as a resonant wavelength shift of the disk resonator, obtaining interesting results. In particular, a deflection sensitivity of 33 nm^{-1}, a detection limit of the slot waveguide disk resonator of 3×10^{-5}nm, an estimated cantilever stress sensitivity of 1.76 nm/(mJ/m^2), that means that the minimum detectable surface stress is $\Delta\sigma_{min}= 1.7\times10^{-5}$ mJ/m^2, have been achieved.

One of the most important aspects for photonic bio-sensing concerns with temperature effects affecting final measurements. The temperature effect is directly linked to very small refractive index changes of the adopted material system. Consequently, the global modal effective index perturbation can be written as:

$$\Delta n_{eff} = \Delta n_{eff,SENSING} \pm \Delta n_{eff,TEMP.} \tag{25}$$

By this way, the resonance wavelength of the ring resonator can change not only due to sensing principles (e.g., homogenous or surface sensing), but also due to temperature changes. The final result is a corrupted measure of biological analytes and molecules to be detected. Three approaches have been used for thermal noise reduction: active temperature control, a-thermal waveguide design, and temperature drift compensation by on chip referencing.

In this context, an on-chip temperature compensation in an integrated slot waveguide ring resonator refractive index sensor array has been investigated (Gylfanson et al., 2010). Experimental study has demonstrated a low temperature dependence of -16.6 pm/K while, at the same time, a large refractive index sensitivity of 240±10 nm/RIU. Furthermore, by using on chip temperature referencing, a differential temperature sensitivity of only 0.3 pm/K has been obtained, without any individual sensor calibration. This low value indicates good sensor-to-sensor repeatability, thus enabling use in highly parallel chemical assays. The detection limit has been demonstrated to be 8.8×10^{-6} RIU in a 7K temperature operating windows. Another interesting solution to the problem of temperature effects in SOI wire waveguide ring resonator label-free biosensor arrays, has been proposed (Xu et al., 2010). The device is constituted by four ring resonators with a reference ring for tracking sensor temperature changes. The reference ring is protected by a 2μm-thick upper cladding layer and optically isolated from the sensing medium. By this way, real-time measurements have shown that the reference resonator resonances are linked to the temperature changes without any noticeable time delay, enabling an effective cancellation of temperature-induced shifts. A concentration of 20pM has been demonstrated by monitoring the binding between complementary IgG protein pairs. In particular, the sensor is able to detect a fluid refractive index fluctuation of $\pm 4\times10^{-6}$. Better results have been achieved by using an array of 32 silicon ring resonator sensors integrated on the same platform.

With a bulk refractive index sensitivity of 7.6×10^{-7} it is possible to detect a concentration of ~ 60fM, by using immobilized biotin to capture streptavidin diluted in bovine serum albumin solution (Iqbal et al., 2010).

In conclusion, a folded cavity SOI micro-ring sensor characterized by a folded spiral path geometry with a 1.2mm long ring waveguide, enclosed in a 150μm diameter sensor area, has been designed (Xu et al., 2008). The spiral cavity resonator is used to monitor the streptavidin protein binding with a detection limit of ~3 pg/mm^2, or a total mass of ~5fg.

The sensor presented above is characterized by Q-factor of 90,650 and an extinction ratio of 8.60 dB.

3.5.1 Resonant architectures for high performance photonic chemical sensing

Due to the increasing demand of high sensitivity and high limit of detection in biological and chemical detections, many kinds of sophisticated photonic sensors have been proposed. In particular, the minimum detectable wavelength shift for a traditional ring sensor is given by the resonance linewidth and resolution of the optical spectra analysis (OSA). In order to achieve ultra high limit of detection, very high resolution optical spectrum analysis and very stable tunable lasers have to be usually used for the whole measurement setup, usually not convenient and very expensive. An innovative approach consists in the joint use of two resonance cavities, for example a ring resonator or a racetrack integrated inside a Fabry-Perot cavity or two ring resonators integrated in the same photonic chip (Fig. 22a). By this way, interesting ultra high performance have been demonstrated.

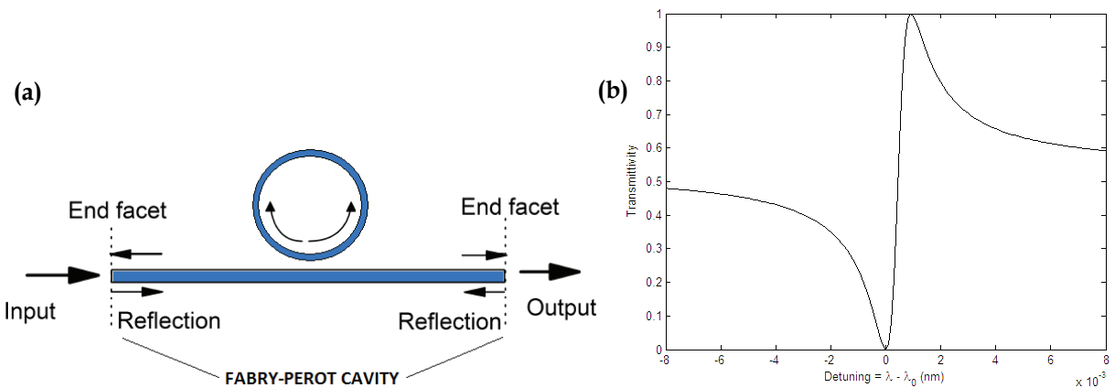

Fig. 22. (a) Micro ring resonator integrated inside a Fabry-Perot resonance cavity.
(b) Illustration of the asymmetric Fano line-shape.

The Fano resonance is due to complex interference present in the structure, as formed by the Fabry-Perot cavity between the reflecting elements and the ring resonator. In Fig. 22b, a typical Fano line-shape has been calculated by considering a silicon ring resonator characterized by a 30μm-long radius, integrated between two reflecting Bragg gratings with a reflection coefficient equal to 0.75. In addition, the central resonant wavelength has been imposed to be λ_0 = 1.535μm. Fano line-shape is characterized by a resonant peak steeper than the Lorentzian's one, that can be obtained with a standard ring resonator (Fig. 21b). By this way, the resolution of the photonic device and the limit of detection are improved. The improvement in terms of sensor performance is obtained because in Fano resonance the slope of the line-shape is greater than that obtained with Lorentzian resonance. To this purpose, a highly sensitive silicon micro-ring sensor with sharp asymmetrical resonance has been presented in literature (Yi et al., 2010). Coupled waveguides and micro-ring resonator have been fabricated using a SOI wafer which has a 1μm buffered oxide layer topped with 230nm of Si. Using a Fabry-Perot cavity characterized by a cavity length of 10mm, a quality factor Q = 3.8×10^4 and a limit of detection of ~10^{-8} have been measured.

The second approach allowing to ensure an ultra-sensitivity and the reduction of the detector complexity, consists in the integration of two cascaded ring resonators in the same chip. The principle used in this configuration is called "Vernier-scale" or "Vernier-effect". It consists of two wavelength scales with different periods, of which one slides the other one. The overlap between lines of two scales is used to perform the measurements.

In Fig. 23, two resonators with different optical roundtrip lengths ($R_2 < R_1$) are cascaded, so that drop signal of the first ring resonator serves as the input for the second one.

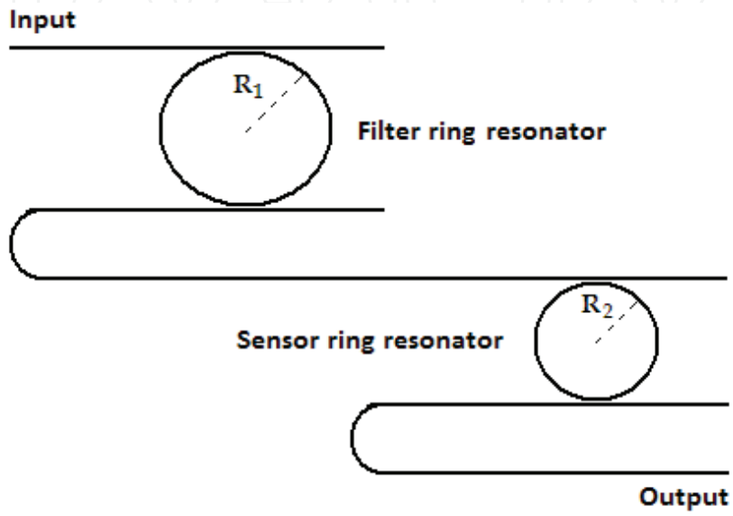

Fig. 23. Schematic view of a cascaded double ring photonic sensor based on Vernier effect.

Each individual ring resonator has a comb-like transmission spectrum with peaks at its resonance wavelengths, as already seen. The transmission spectrum of the cascade of two ring resonators is the product of the transmission spectra of the isolated individual resonators. Consequently, it will only exhibit peaks at wavelengths for which two resonance peaks of the respective ring resonators overlap, and the height of each of these peaks will be determined by the amount of this overlap. The sensor ring resonator will act as the sliding part of the Vernier-scale, as its evanescent field can interact with the refractive index in the environment of the sensor, where a change will cause a shift of the resonance wavelengths. The filter ring resonator is shielded from these refractive index changes by the cladding and will act as the constant part of the Vernier-scale. By this way, the whole architecture can be designed such that a small shift of the resonant wavelengths of the sensor ring resonator will result in a much larger shift of the transmission spectrum of the cascade. To this purpose, very interesting results have been demonstrated by using a silicon photonic biosensor whom architecture is the same as that sketched in Fig. 23 (Claes et al., 2010). The sensor has been tested with three aqueous solutions of NaCl with different concentrations and the operative wavelength range is from 1.52μm to 1.54μm. A sensitivity of 2169 nm/RIU has been experimentally determined in aqueous environment. In addition, the minimum detectable wavelength shift $\Delta\lambda$ is 18pm and the LOD is 8.3×10^{-6} RIU.

In conclusion, both integrated architectures analyzed above, can be designed by adopting slot waveguides in order to further improve their performance.

4. Conclusions

Photonic sensors represent a real revolution in chemical sensing technologies. In fact, their most important features are:

- Extremely high selectivity and sensitivity;
- Multi-variable and parallel processing in a chip;
- Wavelength readout (noise and interference immunity);
- Low-cost and high integration with front-end and support electronic systems (silicon, CMOS-compatible processing);
- Real-time processing.

In addition, the silicon-on-insulator technology platform allows to integrate photonics (laser, sensing architecture, photo-detector) and electronics (CMOS data processing) on the same chip in partially monolithic form to constitute the so called Lab-on-a-chip photonic system. Moreover, the refractive index contrast of the Si/SiO_2 material system, enables record reduction in photonic device footprint with ultra-high performance and portability. Undoubtedly, photonic Lab-on-a-chip represents the innovative approach to the main mission of the modern age: the improvement of the human life quality.

Finally, a comparative Table is presented below in order to appreciate all features and performance of actual different photonic sensor configurations.

Architecture	Technology	Performance	Size	Analyte	Author
MZI	SOI	8.7×10^{-7} RIU/ppm	2.1mm-long	BTEX	Saunders et al., 2010
MZI	CMOS-compatible	0.3 pg/mm^2	1.8mm-long (×9 - array)	IgG goat ,rabbit	Densmore et al., 2009
SPR	CMOS-compatible	3022nm/RIU 70pg/mm^2	~ 800µm^2	Molecules	DiPippo et al., 2010
Grating	SOI	~ 120nm ~ 10^{-4}RIU	173µm-long	Biological reactions	Passaro et al., 2008
PhC-slot	SOI	100ppm	300µm-long	Methane	Lai et al., 2011
PhC-slot	SOI	510nm/RIU 1×10^{-5}RIU	2µm-cavity length	Gases N_2, He, CO_2	Jagerska et al., 2010
Directional coupler	SOI	0.1 g/L	~ 1mm^2 (footprint)	Glucose	Passaro et al., 2009
MMI	SOI	+152, -172	1.607µm-long	Glucose, etanole	McCosker & Town, 2010b
Slot-ring resonator	SOI	2000nm/RIU 3.8×10^{-5}RIU	~ 1mm^2 (footprint)	Molecules, Gases	Passaro et al., 2011
Ring resonator	SOI	60fM	175×500µm^2 (×32- array)	DNA	Iqbal et al., 2010
Cascaded resonators	SOI	2169nm/RIU 8.3×10^{-6}RIU	200×70µm^2 (2x- array)	NaCl, molecules	Claes et al., 2010

Table 2. Comparative analysis of several silicon photonic platforms optimized for chemical and biochemical sensing.

5. Acknowledgments

This work has been supported by Fondazione della Cassa di Risparmio di Puglia, Bari, Italy.

6. References

Almeida, V.R.; Xu, Q.; Barrios, C.A. & Lipson, M. (2004). Guiding and confining light in void nanostructure. *Optics Letters,* Vol.29, No.11, (June 2004), pp. 1209-1211

Arshak, K.; Velusamy, V.; Korostynska, O.; Oliwa-Stasiak, K. & Adley, C. (2009). Conducting Polymers and Their Applications to Biosensors: Emphasizing on Foodborne Pathogen Detection. *IEEE Sensors Journal*, Vol.9, No.12, (December 2009), pp. 1942-1951

Baehr-Jones, T.; Hochberg, M.; Walker, C. & Scherer, A. (2005). *Applied Physics Letters*, Vol.86, No.8, (February 2005), art. 081101

Barrios, C.A. (2006). Ultrasensitive Nanomechanical Photonic Sensor Based on Horizontal Slot-Waveguide Resonator", *IEEE Photonic Technology Letters*, Vol.18, No.22, (November 2006), pp. 2419-2421

Bettotti, P.; Pitanti, A.; Rigo, E.; De Leonardis, F.; Passaro, V.M.N. & Pavesi, L. (2011). Modeling of Slot Waveguide Sensors Based on Polymeric Materials. *Sensors*, Vol.11, No.8, (August 2011), pp. 7327-7340

Claes, T.; Bogaerts, W. & Bienstam, P. (2010). Experimental characterization of a silicon photonic sensor consisting of two cascaded ring resonators based on the Vernier-effect and introduction of a curve fitting method for an improved detection limit. *Optics Express*, Vol.18, No.22, pp. 22747-22761

De Leonardis, F. & Passaro, V.M.N. (2007). Modeling and Performance of a Guided-Wave Optical Angular Velocity Sensor based on Raman Effect in SOI, *IEEE J. Lightwave Technol*., Vol.25, No.9, (September 2007), pp. 2352-2366

De Leonardis, F.; Giannoccaro, G.; Troia, B.; Passaro, V.M.N. & Perri, A.G. (2011). Design of Optimized SOI Slot Waveguides for Homogeneous Optical Sensing in Near Infrared. *Int. Workshop on Sensors and Interfaces (IWASI 2011)*, ISBN: 978-1-4577-0624-0, pp. 142-147, June 28-29, 2011

Dell'Olio, F. & Passaro, V.M.N. (2007). Optical sensing by optimized silicon slot waveguides. *Optics Express*, Vol.15, No.8, (April 2007), pp. 4977-4993

Densmore, A.; Vachon, M.; Xu, D.-X.; Janz, S.; Ma, R.; Li, Y.-H.; Lopinski, G.; Delage, A.; Lapointe, J.; Luebbert C.C.; Liu, Q.Y.; Cheben, P. & Schmid J.H. (2009). Silicon photonic wire biosensor array for multiplexed real-time and label free molecular detection. *Optics Letters*, Vol.34, No.23, (November 2009), pp. 3598-3600

DiPippo, W.; Jae Lee, B. &Park, K. (2010). Design analysis of doped-silicon Plasmon resonance immunosensors in mid-infrared range. *Optics Express*, Vol.18, No.18, (August 2010), pp. 19396-19406

Gylfason, K.B.; Carlborg, C.F.; Kazmierczak, A.; Dortu, F.; Sohlstrom, H.; Vivien, L.; Barrios, C.A.; Van Der Wijngaart, W. & Stemme, G. (2010). On-chip temperature compensation in an integrated slot waveguide ring resonator refractive index sensor array. *Optics Express*, Vol.18, No.4, (February 2010), pp. 3226-3237

Hu, S.; Liu, F.; Wan, R. & Huang, Y. (2010). Coupling characteristics between slot plasmonic mode and dielectric waveguide mode. *Communications and Photonics Conference and Exhibition (ACP)*, ISBN: 978-1-4244-7111-9, December 8-12, 2010

Iqbal, M.; Zheng, Z. & Jiansheng, L. (2008). Microwave and Millimeter Wave Technology, *Proceedings of ICMMT*, pp. 878-881, ISBN 978-1-4244-1879-4, April 21-24, 2008

Iqbal, M.; Gleeson, M.A.; Spaugh, B.; Tybor, F.; Gunn, W.G.; Hochberg, M.; Baehr-Jones, T.; Bailey, R.C. & Gunn, L.C. (2010). Label-Free Biosensor Arrays Based on Silicon Ring Resonators and High-Speed Optical Scanning Instrumentation. *IEEE Journal of Selected Topics in Quantum Electronics*. Vol.16, No.3, (May-June 2010), pp. 654-661

Jagerska, J.; Zhang, H.; Diao, Z.; Le Thomas, N. & Houdrè, R. (2010). Refractive index sensing with an air-slot photonic crystal nanocavity. *Optics Letters*, Vol.35, No.15, (August 2010), pp. 2523-2525

Jha, R. & Sharma, A.K. (2010). Design of a silicon-based plasmonic biosensor chip for human blood-group identification. *Sensors and Actuators B: Chemical*, Vol.145, No.1, (March 2010), pp. 200-204

Kargar A. & Lee C. (2009). Optical sensing by multiple-slot waveguide microring resonators. *9th IEEE Conference on Nanotechnology*. ISBN: 978-1-4244-4832-6, July 26-30, 2009

Kuo, W.-K. & Chang C.-H. (2010). Phase detection properties of grating-coupled surface Plasmon resonance sensors. *Optics Express*, Vol.18, No.19, (September 2010), pp. 19656-19664

Lai, W.-C.; Chakravarty, S.; Wang, X.; Lin, C. & Chen, R.T. (2011). On-chip methane sensing by near-IR absorption signatures in a photonic crystal slot waveguide. *Optics Letters*, Vol.36, No.6, (March 2011), pp. 984-986

Le, L.; Suihua, M.; Yanhong, J.; Xinyuan, C.; Zhiyi, L.; Yonghong, H. & Jihua, G. (2011). A two-dimensional polarization interferometry based parallel scan angular surface plasmon resonance biosensor. *Review of Scientific Instruments*, Vol.82, No.2, (February 2011), art. 023109

Lee, S.M.; Saini, S.S. & Jeong, M.Y. (2010). Parametric Discrimination between Refractive Index, Temperature and Strain using Etched-Core FBG. *23rd Annual Meeting of the IEEE Photonics Society*, ISBN: 978-1-4244-5368-9, November 7-11, 2010

Leheny, R.F. & McCants, C.E. (2009). Technologies for Photonic Sensor Systems, *Proceedings of the IEEE*, Vol.97, No.6, (June 2009), pp. 957-970

Li, S.; Yin, S.; Jiang, Y.; Yin, C; Deng, Q. & Du, C. (2010). Specific Protein Detection in Multiprotein Coexisting Environment by Using LSPR Biosensor. *IEEE Transactions on Nanotechnology*, Vol.9, No.5, (September 2010), pp. 554-557

Malathi, S.; Rani, K.E. & Srinivas, T. (2010). Design and analysis of SOI based biosensor with integrated optic readout. *Computing Communication and Networking Technologies*, ISBN: 978-1-4244-6591-0, July 29-31, 2010

Marrocco, V.; Vincenti, M.A.; Grande, M.; Calò, G.; Petruzzelli, V.; Prudenzano F. & D'Orazio, A. (2010). Field localization in Bragg waveguide assisted by metal layers. *Journal of the Optical Society of America B*, Vol.27, No.4, (March 2010), pp. 703-707

McCosker, R.J. & Town, G.E. (2010a). Optical chemical sensor using a multi-channel directional coupler with slot waveguides. *International Conference on Photonics (ICP)*, ISBN: 978-1-4244-7186-7, July 5-7, 2010

McCosker, R.J. & Town, G.E. (2010b). Multi-channel directional coupler as an evanescent field sensor. (2010). *Sensors and Actuators B: Chemical*, Vol.150, No.1, (September 2010), pp. 417-424

Passaro, V.M.N.; Dell'Olio, F.; Casamassima, B. & De Leonardis, F. (2007a). Guided-Wave Optical Biosensors, *Sensors*, Vol.7, No.4, (April 2007), pp. 508-536

Passaro, V. M. N.; Dell'Olio, F. & De Leonardis, F. (2007b). Ammonia Optical Sensing by Microring Resonators. *Sensors*, Vol.7, No.11, (November 2007), pp. 2741-2749

Passaro, V.M.N.; Loiacono, R.; D'Amico, G. & De Leonardis, F. (2008). Design of Bragg Grating Sensors Based on Submicrometer Optical Rib Waveguides in SOI. *IEEE Sensors Journal*, Vol.8, No.9, (September 2008), pp. 1603-1611

Passaro, V.M.N. (2009a). *Modeling of Photonic Devices*, NOVA Science Publ., ISBN: 978-1-60456-980-3, New York, USA

Passaro, V.M.N.; Dell'Olio F.; Ciminelli C. & Armenise M.N. (2009b). Efficient Chemical Sensing by Coupled Slot SOI Waveguides. *Sensors*, Vol.9, No.2, (February 2009), pp. 1012-1032

Passaro, V.M.N.; Troia, B.; De Leonardis, F. (2011). Group IV Photonic Slot Structures for Highly Efficient Gas Sensing in mid-IR, *IARIA Int. Conference on Sensor Device Technologies and Applications (SENSORDEVICES 2011)*, Nizza (FR), ISBN: 978-1-61208-145-8, August 21-27, 2011

Saunders, J.; Dreher, M.A.; Barnes, J.A.; Crudden, C.M.; Du, J.; Loock, H.; Dan-Xia Xu; Densmore, A.; Ma, R.; Janz, S.; Vachon, M.; Lapointe, J.; Delage, A.; Schmid, J. & Cheben, P. (2010). Detection of lead contamination of water and VOC contamination of air using SOI micro-optical devices. *7th IEEE International Conference on Group IV Photonics.* ISBN: 978-1-4244-6344-2, 1-3 September 2010

Sun, R.; Dong, P.; Feng, N.; Hong, C.; Michel, J.; Lipson, M. & Kimerling, L. (2007). Horizontal single and multiple slot waveguides: optical transmission at λ = 1550nm. *Optics Express*, Vol.15, No.26, (December 2007), pp. 17967-17972

Sun, H.; Chen, A. & Dalton, L.R. (2009). Enhanced Evanescent Confinement in Multiple-Slot Waveguides and Its Application in Biochemical Sensing. *IEEE Photonics Journal*, Vol.1, No.1, (June 2009), pp. 48-57

Troia, B.; Passaro, V. M. N. & De Leonardis, F. (2011). Bandgap Engineering and Optical Properties of Group IV Material Compounds, *Proceedings of 13° Nat. Conf. of Photonic Technologies (Fotonica 2011)*, ISBN: 978-8-8872-3712-2, Genova, Italy, May 9-11, 2011

Tung, B.T.; Dao, V.D.; Ikeda, T.; Kanamori, Y.; Hane, K. & Sugiyama S. (2011). Investigation of strain sensing effect in modified single-defect photonic crystal nanocavity. *Optics Express*, Vol.19, No.9, (April 2011), pp. 8821-8829

Xu, D.-X.; Densmore, A.; Delage, A.; Waldron, P.; McKinnon, R.; Janz, S.; Lapointe, J.; Lopinski, G.; Mischki, T.; Post, E; Cheben, P. & Schmid, J.H. (2008). Folded cavity SOI microring sensors for high sensitivity and real time measurement of

biomolecular binding. *Optics Express*, Vol.16, No.19, (September 2008), pp. 15137-15148

Xu, D.-X.; Vachon, M.; Densmore, A.; Ma, R.; Janz, S.; Delage, A.; Lapointe, J; Cheben, P.; Schmid, J.H.; Post, E.; Messaoudene, S. & Fedeli, J.-M. (2010). Real-time cancellation of temperature induced resonance shifts in SOI wire waveguide ring resonator label-free biosensor arrays. *Optics Express*, Vol.18, No.22, (October 2010), pp. 22867-22879

Yi, H.; Citrin, D.S. & Zhou, Z. (2010). Highly sensitive silicon microring sensor with sharp asymmetrical resonance. *Optics Express*, Vol.18, No.3, (February 2010), pp. 2967-2972

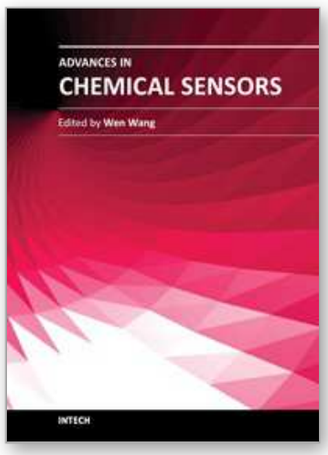

Advances in Chemical Sensors

Edited by Prof. Wen Wang

ISBN 978-953-307-792-5
Hard cover, 358 pages
Publisher InTech
Published online 20, January, 2012
Published in print edition January, 2012

The chemical sensor plays an essential role in the fields of environmental conservation and monitoring, disaster and disease prevention, and industrial analysis. A typical chemical sensor is a device that transforms chemical information in a selective and reversible way, ranging from the concentration of a specific sample component to total composition analysis, into an analytically useful signal. Much research work has been performed to achieve a chemical sensor with such excellent qualities as quick response, low cost, small size, superior sensitivity, good reversibility and selectivity, and excellent detection limit. This book introduces the latest advances on chemical sensors. It consists of 15 chapters composed by the researchers active in the field of chemical sensors, and is divided into 5 sections according to the classification following the principles of signal transducer. This collection of up-to-date information and the latest research progress on chemical sensor will provide valuable references and learning materials for all those working in the field of chemical sensors.

How to reference

In order to correctly reference this scholarly work, feel free to copy and paste the following:

Vittorio M. N. Passaro, Benedetto Troia, Mario La Notte and Francesco De Leonardis (2012). Chemical Sensors Based on Photonic Structures, Advances in Chemical Sensors, Prof. Wen Wang (Ed.), ISBN: 978-953-307-792-5, InTech, Available from: http://www.intechopen.com/books/advances-in-chemical-sensors/chemical-sensors-based-on-photonic-structures

INTECH
open science | open minds

InTech Europe
University Campus STeP Ri
Slavka Krautzeka 83/A
51000 Rijeka, Croatia
Phone: +385 (51) 770 447
Fax: +385 (51) 686 166
www.intechopen.com

InTech China
Unit 405, Office Block, Hotel Equatorial Shanghai
No.65, Yan An Road (West), Shanghai, 200040, China
中国上海市延安西路65号上海国际贵都大饭店办公楼405单元
Phone: +86-21-62489820
Fax: +86-21-62489821

IntechOpen